

# The inner dark matter distribution of the Cosmic Horseshoe (J1148+1930) with gravitational lensing and dynamics

S. Schuldt<sup>1,2</sup>, G. Chirivì<sup>1</sup>, S. H. Suyu<sup>1,2,3</sup>, A. Yıldırım<sup>1,4</sup>, A. Sonnenfeld<sup>5</sup>, A. Halkola<sup>6</sup>, and G. F. Lewis<sup>7</sup>

<sup>1</sup> Max-Planck-Institut für Astrophysik, Karl-Schwarzschild Str. 1, 85741 Garching, Germany  
e-mail: schuldt@mpa-garching.mpg.de

<sup>2</sup> Physik Department, Technische Universität München, James-Franck Str. 1, 85741 Garching, Germany

<sup>3</sup> Institute of Astronomy and Astrophysics, Academia Sinica, P.O. Box 23-141, Taipei 10617, Taiwan

<sup>4</sup> Max Planck Institute for Astronomy, Königstuhl 17, 69117 Heidelberg, Germany

<sup>5</sup> Kavli Institute for the Physics and Mathematics of the Universe, The University of Tokyo, 5-1-5 Kashiwanoha, Kashiwa, 277-8583

<sup>6</sup> Pyörrekuja 5 A, 04300 Tuusula, Finland

<sup>7</sup> Sydney Institute for Astronomy, School of Physics, A28, The University of Sydney, NSW 2006, Australia

Received –; accepted –

## ABSTRACT

We present a detailed analysis of the inner mass structure of the Cosmic Horseshoe (J1148+1930) strong gravitational lens system observed with the *Hubble Space Telescope* (*HST*) Wide Field Camera 3 (WFC3). In addition to the spectacular Einstein ring, this systems shows a radial arc. We obtained the redshift of the radial arc counter image  $z_{s,r} = 1.961 \pm 0.001$  from Gemini observations. To disentangle the dark and luminous matter, we consider three different profiles for the dark matter distribution: a power-law profile, the NFW, and a generalized version of the NFW profile. For the luminous matter distribution, we base it on the observed light distribution that is fitted with three components: a point mass for the central light component resembling an active galactic nucleus, and the remaining two extended light components scaled by a constant M/L. To constrain the model further, we include published velocity dispersion measurements of the lens galaxy and perform a self-consistent lensing and axisymmetric Jeans dynamical modeling. Our model fits well to the observations including the radial arc, independent of the dark matter profile. Depending on the dark matter profile, we get a dark matter fraction between 60% and 70%. With our composite mass model we find that the radial arc helps to constrain the inner dark matter distribution of the Cosmic Horseshoe independently of the dark matter profile.

**Key words.** Dark Matter – Galaxies: individual: Cosmic Horseshoe (J1148+1930) –galaxies:kinematics and dynamics – gravitational lensing: strong

## 1. Introduction

In the standard cold dark matter (CDM) model, the structure of dark matter halos is well understood through large numerical simulations based only on gravity (e.g., Dubinski & Carlberg 1991; Navarro et al. 1996a,b; Ghigna et al. 2000; Diemand et al. 2005; Graham et al. 2006b; Gao et al. 2012). From these N-body dark matter only simulations it appears that halos are well described by the NFW profile (Navarro, Frenk, & White 1997). This profile has characteristic slopes; it falls at large radii as  $\rho_{r \gg r_s} \propto r^{-3}$ , while, for small radii, it goes as  $\rho_{r \ll r_s} \propto r^{-1}$  and thus forms a central density cusp. The so-called scale radius  $r_s$  is the radius where the slope changes. Nowadays, simulations with higher resolution predict shallower behavior for the density slope at very small radii and thus a deviation from this simple profile (e.g., Golse & Kneib 2002; Graham et al. 2006a; Navarro et al. 2010; Gao et al. 2012). Thus, the distribution is more cored than cuspy (e.g., Collett et al. 2017; Dekel et al. 2017). These simulations are also showing that DM halos are not strictly self-similar as first expected for a CDM universe (e.g., Ryden 1991; Moutarde et al. 1995; Chuzhoy 2006; Lapi & Cavaliere 2011).

In realistic models for halos one has to include the baryonic component, and that modifies the distribution and the amount of dark matter. The distribution of stars, dark matter, and gas depends on processes such as gas cooling, which allows baryons to condense towards the center (e.g., Blumenthal et al. 1986;

Gnedin et al. 2004; Sellwood & McGaugh 2005; Gustafsson et al. 2006; Pedrosa et al. 2009; Abadi et al. 2010; Sommer-Larsen & Limousin 2010), active galactic nuclei (AGNs) feedback (e.g., Peirani et al. 2008; Martizzi et al. 2013; Peirani et al. 2017; Li et al. 2017), dynamical heating in the central cuspy region due to infalling satellites and mergers (e.g., El-Zant et al. 2001, 2004; Nipoti et al. 2004; Romano-Díaz et al. 2008; Tonini et al. 2006; Laporte & White 2015) and thermal and mechanical feedback from supernovae (e.g., Navarro et al. 1996b; Governato et al. 2010; Pontzen & Governato 2012).

Therefore, detailed observations of the mass distribution include important information of these complex baryonic processes. Of particular interest is the radial density profile of DM on small scales. In addition, at small radii we expect to have the densest regions of the DM particles, therefore these regions are ideal to learn more about their interactions and nature (Spergel & Steinhardt 2000; Abazajian et al. 2001; Kaplinghat 2005; Peter et al. 2010).

Strong gravitational lensing has arisen as a good technique to obtain the mass distribution for a wide range of systems. Gravitational lensing provides a measurement of the total mass within the Einstein ring since the gravitational force is independent of the mass nature (e.g., Treu 2010; Treu & Ellis 2015). Dye & Warren (2005) showed that strong lens systems with a nearly-full Einstein ring are better than those observations where the source is lensed into multiple point-like images if one wants to

construct a composite profile of baryons and dark matter. With such observations, one can very well fit the profile near the region of the Einstein ring, but the inner part cannot be well constrained due to the typical absence of lensing data in the inner region. The presence of a radial arc, even though seldom observed in galaxy-scale lenses, can help break the lensing degeneracies and put constraints on the inner mass distribution. Another possibility is to combine lensing and dynamics, which is now a well established probe to get for instance the density profile for early-type galaxies (ETGs; e.g., Mortlock & Webster 2000; Treu & Koopmans 2002, 2004; Gavazzi et al. 2007; Barnabè et al. 2009; Auger et al. 2010; van de Ven et al. 2010; Barnabè et al. 2011; Grillo et al. 2013).

In this paper, we present a detailed study of the inner mass structure of the Cosmic Horseshoe lens through lensing and combine these information with those coming from dynamical modeling. The Cosmic Horseshoe, discovered by Belokurov et al. (2007), is ideal for such a study: the deflector galaxy’s huge amount of mass results in a spectacular and large Einstein ring, and near the center of the lens exists a radial arc, which helps to constrain the mass distribution in the inner part of the Einstein ring. To include the radial arc and our association for its counter image in the models, we have spectroscopy measurements for the counter image to get its redshift.

The outline of the paper is as follows. In Sec. 2 we introduce the imaging and spectroscopic observations with their characteristics and describe the data reduction and redshift measurement for the radial arc counter image. Then we revisit briefly in Sec. 3 the multiple-lens-plane theory. In Sec. 4 we present our results of the composite mass model of baryons and dark matter using lensing-only, while in Sec. 5 we present the results of our models based on dynamics-only. In Sec. 6 we combine lensing and dynamics and present our final models. Sec. 7 summarizes and concludes our results.

Throughout this work, we assume a flat  $\Lambda$ CDM cosmology with Hubble constant  $H_0 = 72 \text{ km s}^{-1} \text{ Mpc}^{-1}$  (Bonvin et al. 2017) and  $\Omega_M = 1 - \Omega_\Lambda = 0.32$  whose values correspond to the updated Planck data (Planck Collaboration et al. 2016). Unless specified otherwise, each quoted parameter estimate is the median of its one-dimensional marginalized posterior probability density function, and the quoted uncertainties show the 16<sup>th</sup> and 84<sup>th</sup> percentiles (that is, the bounds of a 68% credible interval).

## 2. The Cosmic Horseshoe (J1148+1930)

The Cosmic Horseshoe, also known as SDSS J1148+1930, was discovered by Belokurov et al. (2007) within the *Sloan Digital Sky Survey* (SDSS). A color image of this gravitational lensed image is shown in Fig. 1. The center of the lens galaxy G, at a redshift of  $z_d = 0.444$ , lies at ( $11^{\text{h}}48^{\text{m}}33^{\text{s}}.15$ ;  $19^{\circ}30'3''.5$ ) of the epoch J2000 (Belokurov et al. 2007). The tangential arc is a star-forming galaxy at redshift  $z_{s,t} = 2.381$  (Quider et al. 2009) which is strongly lensed into a nearly full Einstein ring ( $\approx 300^\circ$ ), whose radius is around  $5''$  and thus one of the largest Einstein rings observed up to now. This large size shows that this lens galaxy must be very massive. A first estimate of the enclosed mass within the Einstein ring is  $\approx 5 \times 10^{12} M_\odot$  (Dye et al. 2008) and thus the lens galaxy, a luminous red galaxy (LRG), is one of the most massive galaxies ever observed. Apart from the nearly full Einstein ring and the huge amount of mass within the Einstein ring, which makes this observation already unique, the Cosmic Horseshoe observations reveal a radial arc. This radial arc is in the west of the lens, as marked in the green solid box in Fig. 1. We include this radial arc in our models as well as our association of

its counter image, marked with a green dashed box in Fig. 1. For this counter image we have Gemini measurements (see Sec. 2.2) to yield a redshift of  $z_{s,r} = 1.961 \pm 0.001$ . A summary of various properties about the Cosmic Horseshoe is given in Table 1.

## The Cosmic Horseshoe

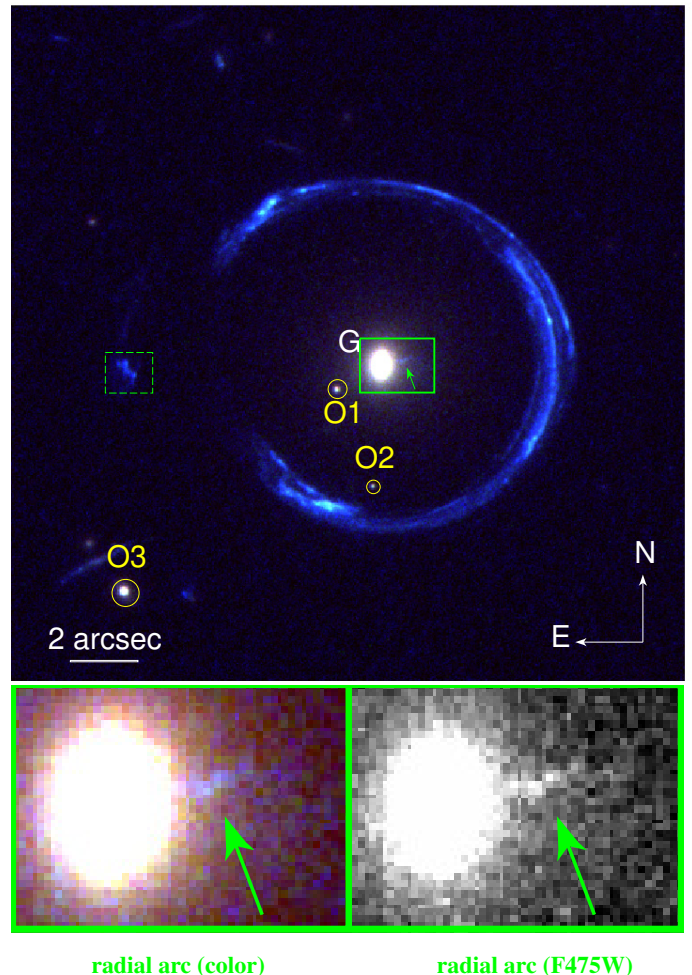


Fig. 1: Color image of the Cosmic Horseshoe obtained through a combination of the F475W, F606W, and F814W filter images from the *HST* WFC3. The size of this image is  $20'' \times 20''$ . One can see the  $\approx 300^\circ$  wide blue Einstein ring of the Cosmic Horseshoe. In addition, the Cosmic Horseshoe observation includes a radial arc which is marked with a green solid box. This is shown in detail in the bottom panel, in color (left) and from the F475W filter (right). We associate this radial arc to its counter image, marked in the main figure with a dashed green box and located around  $8''$  on the east side of the lens galaxy G. Both the radial arc and its counter image correspond to a source at redshift  $z_{s,r} = 1.961$  (see Sec. 2.2). The three star-like objects in the field of view, which we include in our light model, are circled in yellow. The figures are oriented such that North is up and East is left.

### 2.1. Hubble Space Telescope imaging

The data we analyse in this work come from the *Hubble Space Telescope* (*HST*) Wide Field Camera 3 (WFC3) and can be

Table 1: Properties of the Cosmic Horseshoe (J1148+1930)

Component	Properties	Value
Lens	Right ascension <sup>a</sup>	11 <sup>h</sup> 48 <sup>m</sup> 33 <sup>s</sup>
	Declination <sup>a</sup>	19°30′3″.5
	Redshift, $z_d$ <sup>a</sup>	0.444
tangential arc source	Redshift, $z_{s,t}$ <sup>b</sup>	2.381
	Star forming rate <sup>b</sup>	$\approx 100 M_\odot \text{ yr}^{-1}$
Ring	Diameter <sup>a</sup>	10.2″
	Length <sup>a</sup>	$\approx 300^\circ$
	Enclosed mass <sup>c,d</sup>	$\approx 5 \times 10^{12} M_\odot$
radial arc source	Redshift, $z_{s,r}$ <sup>d</sup>	1.961

References:

<sup>a</sup> Belokurov et al. (2007)

<sup>b</sup> Quider et al. (2009)

<sup>c</sup> Dye et al. (2008)

<sup>d</sup> result presented in this paper

downloaded from the Mikulski Archive for Space Telescopes<sup>1</sup>. The observations with filters F475W, F606W, F814W, F110W, and F160W were obtained in May 2010 (PI: Sahar Allam) and the observations with the F275W filter in November 2011 (PI: Anna Quider).

For the data reduction we use *HST* DrizzlePac<sup>2</sup>. The size of a pixel after reduction is 0.04″ for WFC3 UVIS (i.e. the F275W, F475W, F814W and F606W band) and 0.13″ for the WFC3 IR (i.e. the F160W and F110W band), respectively. The software includes a sky background subtraction. In our case the subtracted background appears to be overestimated since many of the pixels have negative value, possibly due to the presence of a very bright and saturated star in the lower-right corner of the WFC3 field of view ( $\approx 160'' \times 160''$ ). Since negative intensity is unphysical and we fit the surface brightness of the pixels, we subtract the median of an empty patch of sky that we pick to be around 25″-N-E to the Cosmic Horseshoe from all pixels of the reduced F160W-band image. After our background correction, around 300 pixels ( $\approx 1.3\%$  of the full cutout) of the corrected image still have negative values, which is consistent with the number given by background noise fluctuations. We proceed in a similar way with the F475W band, where the number of negative pixel is still high but in the range of background fluctuations.

To align the images of the different filters we are using in this paper, we model the light distribution of the star-like objects O2 and O3 (see Fig. 1) in the F475W band, masking out all the remaining light components (such as arc, lens and object O1). We do not include object O1 in the alignment since we do not model the light distribution of the lens in this band and the lens has significant flux in the region of O1 that could affect the light distribution of O1. From this model and our lens light model in the F160W band, which we present in Sec. 4.2.1, we get the coordinates of the centers of both objects in the two considered bands. Under the assumption these coordinates should match, we are able to align the F475W and the F160W images.

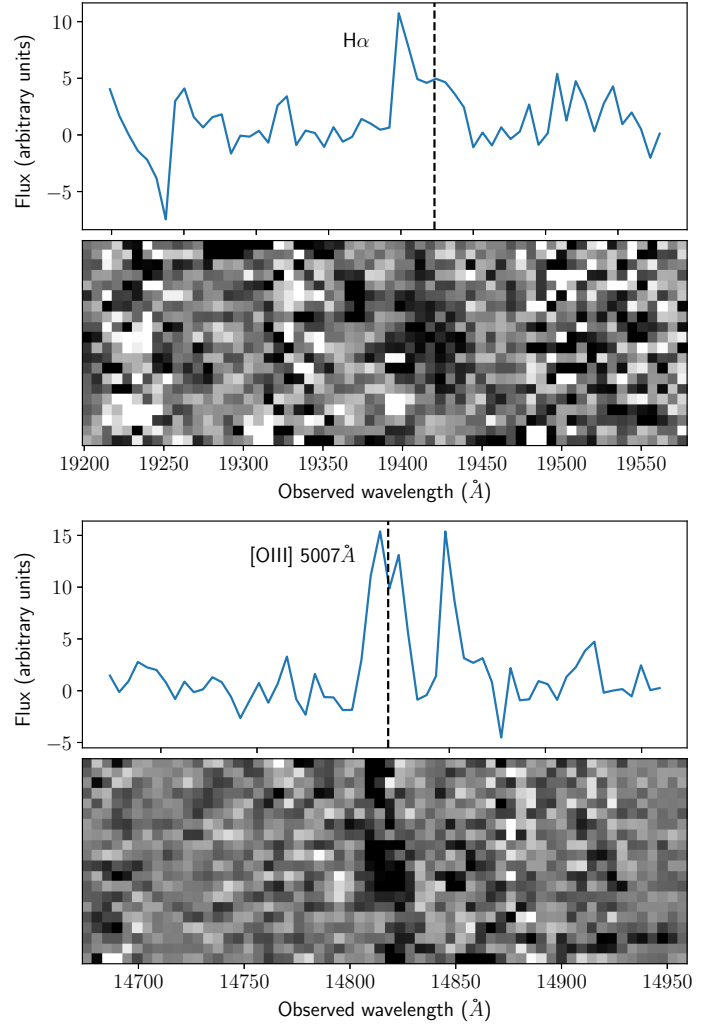


Fig. 2: *Top (Bottom)*: 2d and 1d spectrum around the  $H\alpha$  ( $[OIII] 5007\text{\AA}$ ) emission line from the counter-image to the radial arc, obtained from GNIRS observations. The 1D spectrum is extracted from a 5 pixel, corresponding to 0.75″, aperture around each line. The secondary peak redward of  $[OII]$  visible in the 1D spectrum is due to a cosmic red that was not properly removed in the data reduction process.

## 2.2. Spectroscopy: redshift of the counter image of radial arc

We obtained a spectrum of the counter-image to the radial arc using the Gemini Near-InfraRed Spectrograph (GNIRS; Elias et al. 2006) on the Gemini North Telescope (Program ID: GN-2012B-Q-42, PI Sonnenfeld). We used GNIRS in cross-dispersed mode, with the 32 l/mm grating, the SXD cross-dispersing prism, short blue camera (0.15″/pix) and a  $7'' \times 0.675''$  slit. This configuration allowed us to achieve continuous spectral coverage in the range 9,000 – 25,000Å with a spectral resolution  $R \sim 900$ . We obtained  $18 \times 300s$  exposures, nodding along the slit with an ABBA template.

We reduced the data using the Gemini IRAF package. We identified two emission lines in the 2D spectrum, plotted in Fig. 2: these are  $H\alpha$  and  $[OIII] 5007\text{\AA}$ , at a redshift  $z_{s,r} = 1.961 \pm 0.001$ . From here on, we take this to be the redshift of the radial arc and its counter-image.

<sup>1</sup> <http://archive.stsci.edu/hst/search.php>

<sup>2</sup> DrizzlePac is a product of the Space Telescope Science Institute, which is operated by AURA for NASA.

### 3. Multi-plane Lensing

In this work we employ multi-plane gravitational lensing, given the presence of two sources at different redshifts (corresponding to the tangential and radial arcs, respectively). We therefore briefly revisit in this section the single plane and generalized multi-plane gravitational lens formalism. In the single plane formalism a light ray of a background source is deflected by one single lens whereas, in the multi-plane case, the same light ray is deflected several times by different deflectors at different redshifts (e.g., Blandford & Narayan 1986; Schneider et al. 2006; Gavazzi et al. 2008). The lens equation of the multi-plane lens theory, which gives the relation between the angular position  $\theta_j$  of a light ray in the  $j$ -th lens plane and the angular position in the  $j = 1$  plane, which is the observed image plane, is given by

$$\theta_j(\theta_1) = \theta_1 - \sum_{k=1}^{j-1} \frac{D_{kj}}{D_j} \hat{\alpha}(\theta_k), \quad (1)$$

where  $\theta_N = \beta$  corresponds to the source plane if  $N$  is the number of planes,  $\theta_k$  is the image position on the  $k$ -th plane,  $\hat{\alpha}(\theta_k)$  is the deflection angle on the  $k$ -th plane,  $D_{kj}$  is the angular diameter distance between the  $k$ -th and  $j$ -th plane, and  $D_j$  is the angular diameter distance between us and the  $j$ -th plane. The total deflection angle  $\alpha_{\text{tot}}$  is then the sum over all deflection angles on all planes

$$\alpha_{\text{tot}} = \sum_{k=1}^{N-1} \frac{D_{kN}}{D_N} \hat{\alpha}(\theta_k). \quad (2)$$

In the case of  $N = 2$  the general formula reduces to the well known lens equation for the single plane formalism, namely

$$\beta = \theta - \frac{D_{\text{ds}}}{D_s} \hat{\alpha}(D_d \theta). \quad (3)$$

Here the only lens is at  $\theta = \theta_1$ , the source at  $\beta = \theta_2$ ,  $\hat{\alpha}$  is the (total) deflection angle, and  $D_{\text{ds}}$ ,  $D_s$  and  $D_d$  the distances between deflector (lens) and source, observer and source, and observer and deflector, respectively (e.g. Schneider et al. 2006).

The magnification  $\mu$  is in the multi-plane formalism defined in the same way as in the single plane formalism, namely

$$\mu = \frac{1}{\det A} \quad (4)$$

with the Jacobian matrix

$$A = \frac{\partial \beta}{\partial \theta} = \frac{\partial \theta_N}{\partial \theta_1}. \quad (5)$$

For the surface mass density  $\Sigma(R)$  one needs the convergence  $\kappa$ , sometimes also called the dimensionless surface mass density. In the single-lens plane case, the convergence is

$$2\kappa = \frac{\partial \alpha_1}{\partial \theta_1} + \frac{\partial \alpha_2}{\partial \theta_2} = \nabla_{\theta} \cdot \alpha, \quad (6)$$

where  $\alpha = (D_{\text{ds}}/D_s)\hat{\alpha}$ . This can then be multiplied with

$$\Sigma_{\text{crit}} = \frac{c^2}{4\pi G} \frac{D_s}{D_d D_{\text{ds}}} \quad (7)$$

to derive  $\Sigma(R)$  using the definition of convergence

$$\kappa = \frac{\Sigma(R)}{\Sigma_{\text{crit}}}. \quad (8)$$

We can then compute the average surface mass density with the formula

$$\Sigma(< R) = \frac{\int_0^R \Sigma(R') 2\pi R' dR'}{\pi R^2}. \quad (9)$$

These general equations hold in the single plane case, but for the multi-plane case one defines similar, so-called effective, quantities. For calculating the effective convergence  $\kappa_{\text{eff}}$  one replaces in Eq. 6 the deflection angle  $\alpha$  with the total deflection angle  $\alpha_{\text{tot}}$  from Eq. 2. In analogy to the case above one computes the effective average surface mass density  $\Sigma_{\text{eff}}(< R)$ , now using  $\kappa_{\text{eff}}$  instead of  $\kappa$ . The consequence is that this quantity  $\Sigma_{\text{eff}}(< R)$  is the gradient of the total deflection angle  $\alpha_{\text{tot}}$  instead of a physical surface density.

### 4. Lens mass models

Since the position of an observed gravitationally lensed image depends on both baryonic and dark matter, one can use gravitational lensing as a probe for the total mass, i.e. baryonic and dark matter together. We start with a model of the lensed source positions, i.e. surface brightness peaks in the observed Einstein ring, with a single power-law plus external shear for the total mass. In addition to the main arc, which is the tangential arc, this model includes the radial arc and its counter image and is presented in Sec. 4.1. Based on this, we construct a composite mass model to describe the total mass. To disentangle the visible (baryonic) matter from the dark matter, we model the lens light distribution (see Sec. 4.2.1) which is then scaled by a constant mass-to-light ratio  $M/L$ , for the baryonic mass. Combining the total mass and the baryonic mass, we construct in Sec. 4.2.2 a composite mass model of baryons and dark matter assuming a power-law (Barkana 1998), a NFW profile (Navarro, Frenk, & White 1997), or a generalized NFW profile for the dark matter distribution. We use then a model based on the full *HST* images (Sec. 4.3) to refine our image positions (Sec. 4.4). In these models we always include the radial arc and our assumption for its counter image. Only in the last section with the redefined image positions we treat explicitly models with and without the radial arc as constraints. This would allow us to quantify the additional constraint on the inner dark matter distribution of the Cosmic Horseshoe from the radial arc, which is the primary goal of this paper.

For the modeling, we use GLEE (Gravitational Lens Efficient Explorer), a gravitational lensing software developed by S. H. Suyu and A. Halkola (Suyu & Halkola 2010; Suyu et al. 2012). This software contains several types of lens and light profiles and uses Bayesian analysis such as simulated annealing and Markov Chain Monte Carlo (MCMC) to infer the parameter values of the profiles. The software also employs the EMCEE package developed by Foreman-Mackey et al. (2013) for sampling the model parameters.

#### 4.1. Power-law model for total mass distribution

In this section, we consider a simple power-law model for the total lens mass distribution, which has been shown by previous studies to describe well the observed tangential arc (e.g., Belokurov et al. 2007; Dye et al. 2008; Quider et al. 2009; Bellagamba et al. 2017). This will allow us to compare our model, that includes the radial arc, with previous models. We visually identify and use as constraints six sets of multiple image

positions, where each set comes from a distinct source component. For modeling the lensed source positions we choose the image of the F475W band, since one can distinguish better between the different parts of the Einstein ring and since the arc is bluer than the lens galaxy. This is an indicator that the lens galaxy is fainter and therefore one can better identify multiple images in F475W. Here we use a singular power-law elliptical mass distribution (SPEMD; Barkana 1998) with slope  $\gamma' = 2g+1$  for the lens (where the convergence  $\kappa(\theta) \propto \theta^{\gamma'-1}$ ) with an external shear. We infer the best-fit parameters of this model by minimizing

$$\chi^2 = \sum_{j=1}^{N_{\text{pt}}} \frac{(\theta_j^{\text{obs}} - \theta_j^{\text{pred}})^2}{\sigma_j^2} \quad (10)$$

with GLEE. Here  $N_{\text{pt}}$  is the number of data points,  $\theta_j^{\text{pred}}$  the predicted and  $\theta_j^{\text{obs}}$  the observed image position, with  $\sigma_j$  the corresponding uncertainty of point  $j$ .

This model contains six sets of multiple images in addition to the radial arc and its counter image (see Fig. 6 with refined identifications that will be described in Sec. 4.4). This model has a  $\chi^2$  of 12.6 for the image positions and the best-fit parameter and median values with  $1-\sigma$  uncertainties are given in Table 2. The obtained marginalized and best-fit values for the total mass model are in agreement with models from previous studies (e.g., Dye et al. 2008; Spiniello et al. 2011).

Table 2: Best-fit and marginalized parameter values for the model assuming a power-law profile plus external shear.

component	parameter	best-fit value	marginalized value
power-law	$x$ ["]	10.86	$10.92^{+0.05}_{-0.05}$
	$y$ ["]	9.60	$9.61^{+0.04}_{-0.04}$
	$q$	0.76	$0.78^{+0.04}_{-0.04}$
	$\theta$ [rad]	0.58	$0.51^{+0.07}_{-0.08}$
	$\theta_E$	8.06	$7.6^{+0.5}_{-0.5}$
	$r_c$ ["]	0.01	$0.29^{+0.3}_{-0.3}$
	$\gamma'$	1.7	$2.0^{+0.4}_{-0.2}$
shear	$\gamma_{\text{ext}}$	0.08	$0.07^{+0.02}_{-0.02}$
	$\phi_{\text{ext}}$ [rad]	3.5	$3.2^{+0.2}_{-0.3}$

Note. The parameters  $x$  and  $y$  are centroid coordinates with respect to the bottom-left corner of our cutout,  $q$  is the axis ratio,  $\theta$  is the position angle measured counterclockwise from the  $x$ -axis,  $\theta_E$  is the Einstein radius,  $r_c$  is the core radius,  $\gamma'$  is the slope,  $\gamma_{\text{ext}}$  is the external shear magnitude, and  $\phi_{\text{ext}}$  is the external shear orientation. The constraints for this model are the selected multiple image systems. The best-fit model has an image position  $\chi^2$  of 12.6.

## 4.2. Components for composite mass model

Since the light deflection depends on both the baryonic and the dark matter, we can construct a composite mass model. For the baryonic component, we need a model of the lens light to scale it by a mass-to-light ratio (Sec. 4.2.1). Since we do not have other information to infer the dark matter component, we fit to the data using different types of mass profiles (Sec. 4.2.2).

### 4.2.1. Lens light distribution for baryonic mass

To disentangle the baryonic matter from the dark matter, we need a model of the lens light distribution. For this we mask out all flux from other components such as stars and the Einstein ring in the image of the F160W filter. We then fit the parameters to the observed intensity value by minimizing the  $\chi^2_{\text{lens}}$ , which is defined as

$$\chi^2_{\text{lens}} = \sum_{j=1}^{N_p} \frac{(I_j^{\text{obs}} - \text{PSF} \otimes I_j^{\text{Sersic}})^2}{\sigma_{\text{tot},j}^2}. \quad (11)$$

Here  $N_p$  is the number of pixels,  $\sigma_{\text{tot},j}$  the total noise, i.e. background and Poisson noise (see below for details), of pixel  $j$ , and  $\otimes$  represents the convolution of the point spread function (PSF) and the predicted intensity. It is necessary to take the convolution with the PSF into account due to telescope effects. Here we use a normalized bright star  $\approx 40''$  S-W of the Cosmic Horseshoe lens as the PSF. We subtract also from the PSF a constant to counterbalance the background coming from a very bright object in the field of view which scatters light over the image.

We approximate the background noise  $\sigma_{\text{bkgd}}$  as a constant that is set to the standard deviation computed from an empty region. We also include the contribution of the astrophysical Poisson noise (Hasinoff 2012), which is expressed as a count rate for pixel  $i$

$$\sigma^2_{\text{poisson},i} = \left( \frac{\sigma'_{\text{tot},i}}{t_i} \right)^2 = \left( \frac{\sqrt{d_i t_i}}{t_i} \right)^2 = \left| \frac{d_i}{t_i} \right|, \quad (12)$$

where  $t_i$  is the exposure time,  $d_i$  the observed intensity of pixel  $i$  (in  $e^-$ -counts per second) and  $\sigma'_{\text{tot},i}$  is the total Poisson noise (labeled with an apostrophe as it is not a rate like  $\sigma_{\text{poisson},i}$ ). We include the contribution of the astrophysical Poisson noise only if it is larger than the background noise. We sum the background noise and astrophysical noise in quadrature, such that  $\sigma^2_{\text{tot},j}$  in Eq. (11) is

$$\sigma^2_{\text{tot},j} = \sigma^2_{\text{bkgd},j} + \sigma^2_{\text{poisson},j}. \quad (13)$$

### Sersic

To describe the surface brightness of the Cosmic Horseshoe lens galaxy, we use the commonly adopted Sersic profile (Sersic 1963), which is the generalization of the de Vaucouleurs law (also called  $r^{1/4}$  profile, De Vaucouleurs 1948). For modeling the lens light distribution we choose the observation in the F160W band, since the lens is brighter in F160W than in the other bands, and infrared bands trace better the stellar mass of the lens galaxy.

The best-fit model obtained by using two Sersic profiles and two stellar profiles (in this model we include two star-like objects, labelled object O1 and object O2 in Fig. 1) has  $\chi^2 = 2.73 \times 10^4$  (corresponding to a reduced  $\chi^2$  of 1.74).

### Chameleon

In addition to our lens light distribution model with the Sersic profile, we also model with another type of profile which mimics the Sersic profile well and allows analytic computations of lensing quantities (e.g., Maller et al. 2000; Dutton et al. 2011; Suyu et al. 2014). It is often called chameleon and composed by



a difference of two isothermal profiles:

$$L(x, y) = \frac{L_0}{1+q_L} \left( \frac{1}{\sqrt{x^2+y^2/q_L^2+4w_c^2/(1+q_L)^2}} - \frac{1}{\sqrt{x^2+y^2/q_L^2+4w_t^2/(1+q_L)^2}} \right). \quad (14)$$

In this equation,  $q_L$  is the axis ratio, and  $w_t$  and  $w_c$  are parameters of the profile with  $w_t > w_c$  to keep  $L > 0$ .

By modeling with the chameleon profile we assume the same background noise as using the Sersic profile (see Sec. 4.2.1). Since the model including two isothermal profile sets and two stellar profiles for the two objects, as used above with the Sersic profile, has a  $\chi^2$  of around two times the Sersic- $\chi^2$ , we add a third chameleon profile and get a  $\chi^2$  of  $2.89 \times 10^4$  which corresponds to a reduced  $\chi^2$  of 1.85. In this model we include also objects O1, O2 and O3 (numbering follows Fig. 1), since we want to use the coordinates for the alignment of the two considered bands, F160W and F475W.

We will use both filters in the extended source modeling (see Sec. 4.3) while in the models using identified image positions we only use the F160W band for the lens light fitting. The parameter values of this best-fit model are used for the mass modeling (given in Table 3) and the corresponding image is shown in Fig. 3. The left image shows the observed intensity and the middle the modeled intensity. In the right panel one can see the normalized residuals of this model in a range  $(-7\sigma, +7\sigma)$ . The constant gray regions are the masked-out areas (containing lensed arcs and neighbouring galaxies) in order to fit only to the flux of the lens. Although there are significant image residuals visible in the right panel, the typical baryonic mass residuals (corresponding to the light residuals scaled by  $M/L$ ) would lead to a change in the deflection angle that is smaller than the image pixel size of  $0.''13$  at the locations of the radial arc.

In Fig. 4 we show the contributions of the different components, plotted along the  $x$ -axis of the cutout in units of solar luminosities for comparison of the contribution of the different light profiles. To compare those components' widths to that of the PSF, in the same figure we show the latter (black dotted line) scaled to the lens light of the central component (plotted in red).

To convert the fitted light distribution into the baryonic mass, we assume at first a constant mass-to-light ratio. This means we scale all three light components by the same  $M/L$  value. Additionally, we explore models with different  $M/L$  values for the different components, either two ratios with  $M/L_{\text{central}} = M/L_{\text{medium}}$  or  $M/L_{\text{medium}} = M/L_{\text{outer}}$  and the remaining different, or with three different  $M/L$  values one for each component. These baryonic mass models are considered in the Sections 4.3 and 4.4.1. Furthermore, since the width of the central component, shown in red in Fig 4, is comparably to the PSF's width, and based on our modeling results in Section 4.4.1, we model in Section 6 this central component by a point mass with Einstein radius described by

$$\theta_{E,\text{point}} = \frac{4GM}{c^2 D_d} \quad (15)$$

(where the Einstein radius is defined here for a source at redshift infinity), superseding the model that scales the central component with an  $M/L$ . Here  $G$  is the gravitational constant,  $M$  the point mass,  $c$  the speed of light, and  $D_d$  the distance to the deflector. For the remaining two components (blue and green in Fig. 4) we assume either one or two different mass-to-light ratios to scale the light to a mass.

#### 4.2.2. Dark matter halo mass distribution

In the previous section we have derived the baryonic component by modeling the light distribution. To disentangle the baryonic mass from the dark component, we model the dark matter distribution using three different profiles. At first we use a NFW (Navarro et al. 1997) profile but, since newer simulations predict deviations from this simple profile, we present in addition the best-fit mass model obtained assuming a power-law profile (Barkana 1998, Singular Power-Law Elliptical Mass Distribution) (with parameters  $q$  as axis ratio,  $\theta_E$  as Einstein radius, and  $r_c$  as core radius) and a generalized version of the NFW profile, given by

$$\rho(r) = \frac{\rho_s}{\left(\frac{r}{r_s}\right)^{\gamma_g} \times \left(1 + \frac{r}{r_s}\right)^{3-\gamma_g}}, \quad (16)$$

where  $\gamma_g$  is the inner dark matter slope. The generalized NFW profile reduces to the standard NFW profile in the case  $\gamma_g = 1$ .

We assume an axisymmetric lens mass distribution (axisymmetric in 3 dimensions), and impose the projected orientation of the dark matter profile to be  $0^\circ$  or  $90^\circ$  rotated with respect to that of the projected light distribution. We find that the  $90^\circ$  orientation gives a better  $\chi^2$ , and thus the dark matter halo seems to be prolate, for an axisymmetric system that has its rotation axis along the minor axis of the projected light distribution. Since strong lensing is only sensitive on scales of the Einstein radius, we assume four different values for the scale radius in the NFW and gNFW profile, namely  $r_s \equiv 18.11'', 36.22'', 90.54'',$  and  $181.08''$ . These values correspond to 100 kpc, 200 kpc, 500 kpc, and 1000 kpc, respectively, for the lens redshift in the considered cosmology. We include the mass of the radial arc source in the model, using a singular isothermal sphere (SIS) profile, as this source galaxy's mass will deflect the light coming from the background tangential arc source. The center of this profile is set to the coordinates for the radial arc source which we obtained from the multiplane lensing, calculated by the weighted mean of the mapped positions of the radial arc and its counter image on the redshift plane of the radial arc.

#### 4.3. Extended source modeling

In the next stage of our composite mass model, we reconstruct the source surface brightness (SB) distribution and fit to the observed lensed source light, i.e. the main arc and the radial arc with its counter image. This will help us to refine our image positions afterwards. For this, we start with the mass model obtained in Sec. 4.2.2, which includes the lens light distribution described by the three chameleon profiles scaled with a constant mass-to-light ratio as baryonic mass and a power-law profile for the dark matter halo. We then allow the mass parameters to vary and, for a given set of mass parameter values, GLEE reconstructs the source SB on a grid of pixels (Suyu et al. 2006). This source is then mapped back to the image plane to get the predicted arc. To infer the best-fit parameters, one optimizes with GLEE the posterior probability distribution which is proportional to the product of the likelihood and the prior of the lens mass parameters (we refer to Suyu et al. (2006) and Suyu & Halkola (2010) for more details). The fitting of the SB distribution has

$$\chi_{\text{SB}}^2 = (\mathbf{d} - \mathbf{d}^{\text{pred}})^T C_D^{-1} (\mathbf{d} - \mathbf{d}^{\text{pred}}), \quad (17)$$

where  $\mathbf{d} = \mathbf{d}^{\text{lens}} + \mathbf{d}^{\text{arc}}$  is the intensity values  $d_j$  of pixel  $j$  written as a vector with length  $N_d$ , the number of image pixels, and  $C_D$

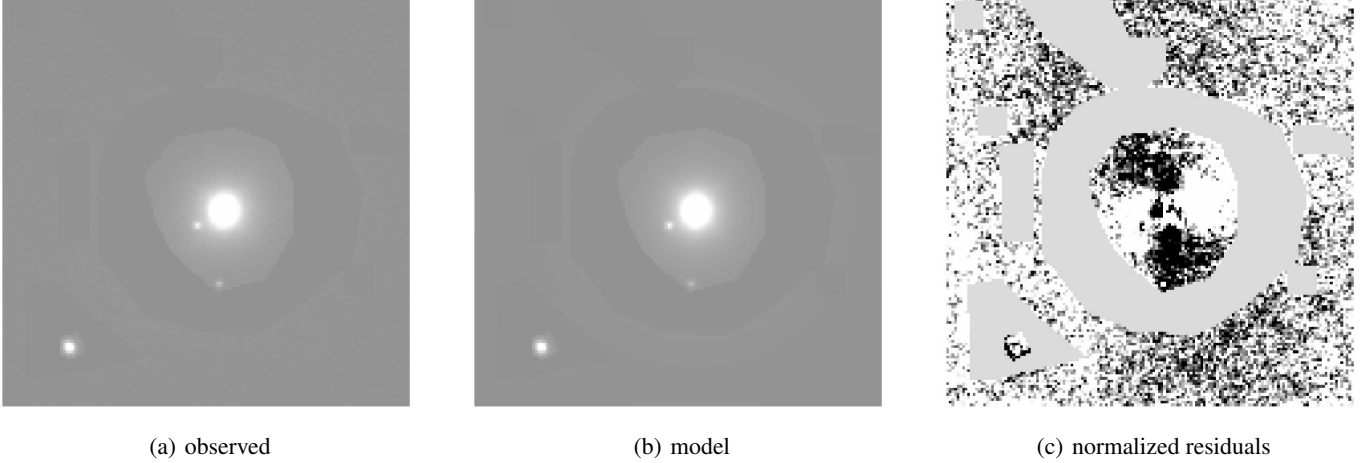


Fig. 3: The best-fit model for the lens light distribution. The left image shows the observation of the Cosmic Horseshoe in the F160W-band, whereas the central panel shows the predicted light distribution. This model includes three chameleon profiles (see Eq. 14) and two PSF and one de Vaucouleurs profiles for the three objects. The right image shows, in a range between  $-7\sigma$  and  $+7\sigma$ , the normalised residuals of this model. The constant gray regions are the masked-out areas (containing lensed arcs and neighboring galaxies) in order to fit only to the flux of the lens. The figures are oriented such that North is up and East is left.

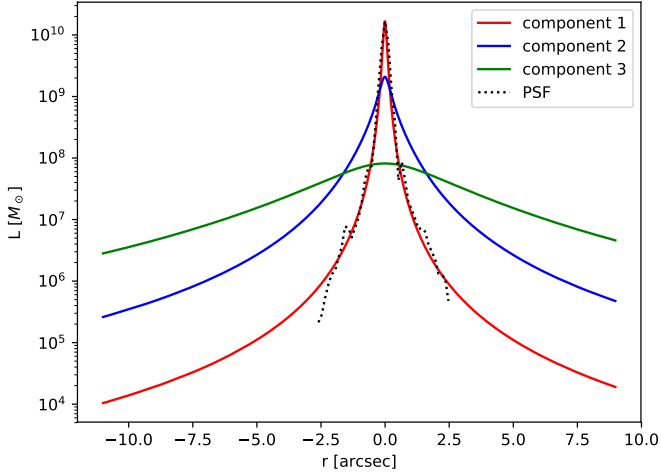


Fig. 4: Different components of the chameleon profiles shown in units of solar luminosity, respectively in red (“inner”), blue (“medium”), and green (“outer” component). The total light observed from the Cosmic Horseshoe lens galaxy in the *HST* filter F160W is described by the sum of all three components. For comparison of the width of the components the scaled PSF is plotted with a black dotted line.

is the image covariance matrix. In the pixellated source SB reconstruction, we impose curvature form of regularization on the source SB pixels (Suyu et al. 2006).

Since we use the observed intensity of the arc to constrain our mass model and the F475W band has the brightest arc relative to the lens light, we include the F475W band in addition to the F160W which is used for the lens light model. For simplicity we assume the same structural parameters of the lens light profiles in the two bands (such as axis ratio  $q$ , center, and orientation  $\theta$ ) and model only the amplitude of the three chameleon profiles and of the three objects included. Explicitly, we model the lens galaxy’s light in both filters and reconstruct the observed intensity of the Einstein ring in both. We also need to specify

and model the radial arc and its counter image separately due to their different redshift from the tangential arc. This is done only in the F475W filter. The light component parameter values of this model, with a  $\chi^2_{\text{SB}}$  of  $7.2 \times 10^4$  for the F160W filter and  $3.1 \times 10^5$  for the F475W filter (the corresponding reduced  $\chi^2_{\text{SB}}$  for the total model is 1.37), are presented in Table 3. In the same table we also give the median values with  $1-\sigma$  uncertainty. The corresponding images of the best-fit model are presented in Fig. 5. In the top row one sees the images of the F160W band, in the middle row the images of the tangential arc and lens light in the F475W band, and in the bottom row the images of the radial arc in the F475W band, respectively. The images are ordered, for each row from left to right, as follows: the first image shows the observed data, the second the predicted, the third image shows the normalized residuals and the fourth image displays the reconstructed source. Despite visible residuals in the reconstruction, some of which are due to finite source pixel size, we are reproducing the global features of the tangential arcs (compare panels a to b, and e to f), to allow us to refine our multiple image positions.

We also model the Cosmic Horseshoe observation with source SB reconstruction assuming the NFW or gNFW for the dark matter halo mass. The fits give for the NFW based model a  $\chi^2_{\text{SB}}$  of  $3.76 \times 10^5$  (corresponding to a reduced  $\chi^2_{\text{SB}} = 1.37$ ) and very similar values for the gNFW model. From this, it seems that the gNFW fits almost as well as the NFW profile. Compared with the power-law extended source model, the  $\chi^2$  is slightly higher, but still comparable. The images reproduce the observations comparably well assuming the power-law profile, as shown in Fig. 5.

#### 4.4. Image position modeling

Finally, we refine multiple image systems using the extended surface brightness modeling results of the last section. This time we find, similarly to what was done in Sec 4.1, eight sets of multiple images systems, in addition to the radial arc and its counter image.

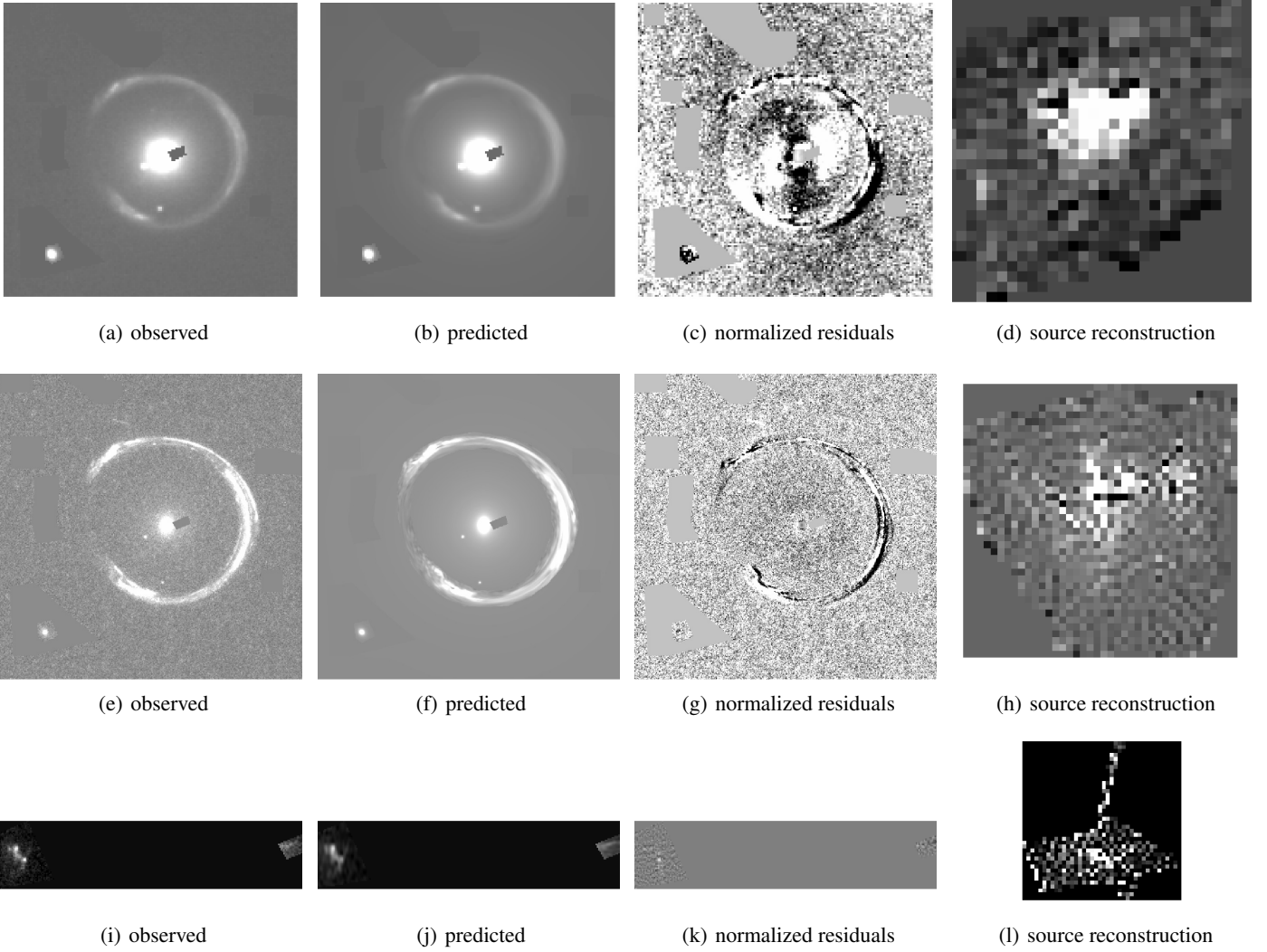


Fig. 5: Images for the best-fit model which includes the source surface brightness reconstruction. In the top row one sees the images of the F160W band, and in the middle (tangential arc with lens) and bottom (radial arc) rows the images of the F475W band, respectively. To separate the radial arc and the tangential arc is needed since they lie at a different redshift. The images are ordered from left to right as follows: observed data, predicted model, normalized residuals in a range from  $-7\sigma$  to  $+7\sigma$  and the reconstructed source SB on a grid of pixels.

#### 4.4.1. Three chameleon profiles

If we assume a constant  $M/L$  for all three chameleon profiles to scale the light to the baryonic mass, our model predicts the positions very well, with a  $\chi^2$  of 20.23, which corresponds to a reduced  $\chi^2$  of 1.07 (in equation 10). Here we use the best-fit model obtained in Sec. 4.3, which adopts the power-law profile, now with core radius set to  $10^{-4}$ , for the dark matter distribution. This is done since the value is always very small and we want to focus on constraining the slope. Another reason is that we need to fix one parameter for our dynamics-only model which is explained more in Sec. 6. The model with the selected multiple image systems is shown in Fig. 6. The figure shows also the critical curves and caustics for both redshifts,  $z_{s,r} = 1.961$  and  $z_{s,t} = 2.381$ , as well as the predicted image positions from GLEE. The filled squares and circles correspond to the model source position (which is the magnification-weighted mean of the mapped source position of each image).

To compare how much constraints we get from the radial arc, we treat also a model based on these image positions excluding

the radial arc and its counter image. Here we have to remove the SIS profile which we adopt for the radial arc source mass. With this model we get a best-fit  $\chi^2$  of 18.87 which corresponds to a reduced  $\chi^2$  of 1.18.

Similarly as before, we test how well we can fit the same multiple image systems, i.e. these eight sets for the tangential arc and the radial arc with its counter image as shown in Fig. 6, with our model by assuming a NFW or gNFW dark matter distribution. It turns out that our model based on the NFW profile gives a  $\chi^2$  of 35.48 (reduced  $\chi^2 = 1.87$ ) whereas the model based on the gNFW profile gives a  $\chi^2$  of 35.19 (reduced  $\chi^2 = 1.96$ ). This means that we do not fit the refined multiple image systems with the NFW or gNFW dark matter distribution as well as with the power-law. We see a big difference in  $\chi^2$  compared to the models where we exclude the radial arc and its counter image. Explicitly, without radial arc are the  $\chi^2$  values 25.44 (reduced  $\chi^2 = 1.59$ ) and 25.40 (reduced  $\chi^2 = 1.70$ ) for the NFW and gNFW profile, respectively.



Table 3: Best-fit and marginalized parameter values for the lens light component of the mass model obtained by reconstructing the source surface brightness.

parameter	Chameleon 1 (lens)		Chameleon 2 (lens)		Chameleon 3 (lens)	
	best-fit value	marginalized value	best-fit value	marginalized	best-fit value	marginalized
$x['']$	11.00	–	11.00	–	11.00	–
$y['']$	9.67	–	9.67	–	9.67	–
$q_L$	0.62	$0.64^{+0.02}_{-0.03}$	1.00	$1.00^{+0.00}_{-0.01}$	1.00	$1.00^{+0.00}_{-0.01}$
$\theta[\text{rad}]$	1.52	–	1.52	–	1.52	–
$L_0$ (F160W)	46.67	–	3.50	–	8.56	–
$w_c$	0.08	$0.07^{+0.01}_{-0.01}$	1.95	$2.04^{+0.06}_{-0.07}$	0.18	$0.20^{+0.03}_{-0.02}$
$w_t$	0.18	$0.18^{+0.01}_{-0.01}$	6.99	$7.01^{+0.03}_{-0.06}$	1.24	$1.31^{+0.02}_{-0.03}$
$L_0$ (F475W)	0.11	$0.11^{+0.01}_{-0.01}$	0.027	$0.029^{+0.001}_{-0.001}$	0.010	$0.010^{+0.001}_{-0.002}$

Note. This model includes three chameleon profiles (see Eq. (14)) for the F160W filter and additionally the same profiles with the same structural parameters for the F475W band. We fix the amplitudes of the F160W band since we are multiplying them with the mass-to-light ratio (variable parameter) in constructing the baryonic mass component.

While the power-law halo model fits well to the image positions, it yields a  $M/L$  of around  $0.4 M_\odot/L_\odot$  that is unphysically low. On the other hand, the NFW and gNFW with a common  $M/L$  for all three light components cannot fit well to the image positions, particularly those of the radial arc. Since newer publications (e.g., Samurović 2016; Sonnenfeld et al. 2018; Bernardi et al. 2018) predict variations in the stellar mass-to-light ratio of massive galaxies, we treat our model of the refined image position models with different mass-to-light ratios for each chameleon profile. Different ratios result in a similar effect as a radial-varying ratio. We treat this variation of different  $M/L$  for all our models, that means both with and without radial arc as well as for all three different dark matter profiles NFW, gNFW and power-law. This will be considered further in Sec. 6.

#### 4.4.2. Central point mass with constant $M/L$ of extended chameleon profiles

Since (1) we get a very small  $M/L$  for the central component (compare red line in Fig. 4) in the previous model, (2) this component is very peaky that the width is smaller as the PSF width, and (3) the Cosmic Horseshoe galaxy is known to be radio active, we infer that the central component is a luminous point component like an AGN. Thus we cannot assume an  $M/L$  for it to scale to the baryonic matter. Therefore we treat also models where we assume a point mass instead of the central light component. The mass range is restricted to be between  $10^8 M_\odot$  and  $10^{10} M_\odot$  as these are the known limits of black hole masses (e.g., Thomas et al. 2016; Rantala et al. 2018). For the two other, extended chameleon profiles, we assume a  $M/L$  to scale them to the baryonic mass. Under this assumption we are able to reproduce a good, physical meaningful model for all three adopted dark matter profiles. Since our final model will also include the kinematic information of the lens galaxy, we will discuss details only for this model in Section 6.

## 5. Kinematics & Dynamics

In Sec. 4 we construct a composite mass model of the Cosmic Horseshoe lens galaxy using lensing alone. In this section we present the kinematic data of the Cosmic Horseshoe lens galaxy taken from Spiniello et al. (2011) and a model based

on dynamics-only (e.g., Yıldırım et al. 2016; Nguyen 2017; Yıldırım et al. 2017; Wang et al. 2018).

For the dynamical modeling we use a software which was further developed by Akın Yıldırım (Yıldırım et al. in prep.) and which is based on the code from Michele Cappellari (Cappellari & Copin 2003; Cappellari 2008). For an overview of the Jeans ansatz and the considered parameterization, the Multi-Gaussian-Expansion (MGE) method, see Appendix 8. We infer the best fit parameters again using EMCEE as already done for the lensing part.

### 5.1. Lens stellar kinematic data

Following the discovery of the famous Cosmic Horseshoe by Belokurov et al. (2007), several follow-up observations were done. In particular, Spiniello et al. (2011) obtained long slit kinematic data for the lens galaxy G in March 2010. This was part of their X-Shooter program (PI: Koopmans). The observations covered a wavelength range from 300 Å to 25000 Å simultaneously with a slit centered on the galaxy, a length of 11'' and a width of 0.''7.

To spatially resolve the kinematic data, they defined seven apertures along the slit and summed up the signal within each aperture. The size of each aperture was chosen to be bigger than the seeing of  $\approx 0.''6$ , such that independent kinematic measurement for each aperture were obtained. These data are listed in Table 4, together with the uncertainties. The obtained weighted average value of the velocity dispersion is  $344 \pm 25 \text{ km s}^{-1}$ . This is within the uncertainty of the measurements. Due to the small number of available data and the huge errors we will consider the symmetrized values and uncertainties as given in Table 4.

For further details on the measurement process or the data of the stellar lens kinematics see Spiniello et al. (2011).

### 5.2. Dynamics-only modeling

Before we combine all available data to constrain maximally the mass of the Cosmic Horseshoe lens galaxy, we model the stellar kinematic data alone. We start from the best-fit model from lensing, and include the parameters anisotropy  $\beta$  and inclination  $i$ . Since we have only seven data points (see Table 4), we can

Table 4: Stellar kinematic data of the Cosmic Horseshoe lens galaxy.

Aperture distance ["]	$v$ [km s <sup>-1</sup> ]	$\sigma$ [km s <sup>-1</sup> ]	$v_{\text{rms}}$ [km s <sup>-1</sup> ]	$v_{\text{rms, sym}}$ [km s <sup>-1</sup> ]
-2.16	$-100 \pm 100$	$350 \pm 100$	$364 \pm 101$	$406 \pm 101$
-1.36	$-80 \pm 100$	$311 \pm 76$	$321 \pm 78$	$340 \pm 89$
-0.64	$-9 \pm 25$	$341 \pm 26$	$341 \pm 27$	$353 \pm 26$
0.00	$0 \pm 12$	$332 \pm 16$	$332 \pm 16$	$332 \pm 16$
+0.64	$62 \pm 18$	$360 \pm 25$	$365 \pm 25$	$353 \pm 26$
+1.36	$77 \pm 80$	$350 \pm 100$	$358 \pm 100$	$340 \pm 89$
+2.16	$180 \pm 100$	$410 \pm 100$	$448 \pm 101$	$406 \pm 101$

Note. We give the distance along the slit measured with respect to the center, the corresponding rotation  $v$  (Spiniello et al. 2011), the velocity dispersion  $\sigma$  (Spiniello et al. 2011), the second velocity moments  $v_{\text{rms}}$  obtained through Eq. (28), and the symmetrized values  $v_{\text{rms, sym}}$ . The uncertainties  $\delta v_{\text{rms}}$  is calculated through the formula  $\delta v_{\text{rms}} = \sqrt{v^2 \delta v^2 + \sigma^2 \delta \sigma^2} / v_{\text{rms}}$ . The last row are the considered values in this section.

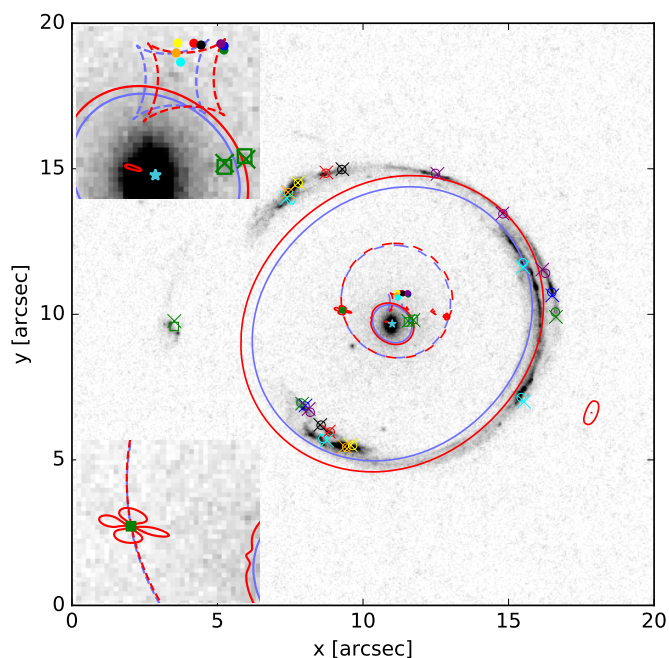


Fig. 6: Best-fit model of the lensed source positions of the Cosmic Horseshoe, which are identified using our best-fit mass model with source SB reconstruction. This model assumes a power-law profile for the dark matter distribution. It is obtained using, as constraints, eight multiple image systems for the Einstein ring (circles) and the radial arc and its counter image (squares). We mark the predicted image positions with a cross. One can see that all predicted images are very close to the selected ones. The blue lines correspond to the critical curves (solid) and caustics (dashed) computed for the redshift of the radial arc, i.e.  $z_{s,r} = 1.961$ , and the red line to the critical curves (solid) and caustics (dashed) computed for the redshift of the tangential arc, i.e.  $z_{s,t} = 2.381$ . The lens position is marked with a blue star. The small additional red features near the radial arc source position, shown in the lower left corner in detail, and on the right hand side are probably due the presence of radial arc source, i.e. as a result of multi-plane lensing. Indeed, we can see that these features do not appear in the single-plane case (blue line). The filled squares and circles correspond to the weighted mean positions of the predicted source position, which are shown in more detail in the zoom in the upper/lower left corner. The figure is oriented such that North is up and East is left.

vary at most six parameters. Thus we set the core radius  $r_c$  of the power-law, which turned out to be very small in our lensing models, to  $10^{-4}$ . For a correct comparison to the refined lensing models (see Sec. 4.4) we fix the core radius there too. For dynamics we will only adopt power-law and NFW dark matter distribution, i.e. no longer the generalization of the NFW profile. The reason is the small improvement compared to the NFW profile. One further reason is that otherwise we have to fix one parameter to vary fewer parameters than the available data points. In other words, for considering the generalized NFW profile we have to fix one parameter such that the number of free parameters is smaller than the number of data points. In analogy to the case of the power-law profile where we fix the core radius, we would set for the generalized NFW profile the slope  $\gamma_g \equiv 1$ . This would result in the NFW profile.

The power-law dark matter distribution gives a dynamics-only best-fit model with  $\chi^2 = 0.25$ . The reason why our model has a  $\chi^2$  much smaller than 1 is due to the big uncertainties. The data points are shown in Fig. 7 (blue) with our dynamics-only model assuming power-law (solid) or NFW (dashed) dark matter distribution. Since we can easily fit to these seven data points in the given range, we treat the same model also with forecasted 5% uncertainties for every measurement. The obtained best-fit dynamics-only model has a  $\chi^2$  of 4.95, which is clearly much higher than for the full error. The best-fit parameter and median values with 1- $\sigma$  uncertainty are given in Table 5 for the model assuming the actual measured errors. As expected, most parameters are within the 1- $\sigma$  range and the mass-to-light ratio is in a good range. The relatively large errors on the parameters are due to the small number of data points we use as constraints.

For the NFW dark matter distribution we fit comparably well as with the power-law model ( $\chi^2 = 0.25$  compared to  $\chi^2 = 0.26$ ), when using the full kinematic uncertainty, while the  $\chi^2$  is slightly higher for the reduced (forecasted 5%) uncertainty on the kinematic data ( $\chi^2 = 4.95$  compared to  $\chi^2 = 5.61$ ). Comparing power-law and the NFW, we do not find a remarkable difference, apart for the radius, which appears to be lower in the NFW forecasted case. This, however, is in agreement with the higher  $\chi^2$  of the NFW since the predicted  $v_{\text{rms}}$  values are in both versions, power-law and NFW profile, lower than the measurement. For a further detailed analysis based on dynamics-only spatially, resolved kinematic measurements would be helpful.

Table 5: Best-fit parameter values for our model based on the power-law dark matter distribution with dynamics-only.

component	parameter	best-fit value	marginalized
kinematics	$\beta$	0.10	$0.01^{+0.2}_{-0.3}$
	$i$	0.1	$0.1^{+0.2}_{-0.2}$
dark matter (power-law)	$q$	0.82	$0.83^{+0.2}_{-0.09}$
	$\theta_E$ ["]	2.3	$2.4^{+0.5}_{-0.4}$
	$r_c$ ["]	$\equiv 10^{-4}$	–
	$\gamma'$	1.20	$1.36^{+0.4}_{-0.2}$
baryonic matter	$M/L [M_\odot/L_\odot]$	1.8	$1.6^{+0.4}_{-0.6}$

Note. The parameters are the anisotropy  $\beta$ , the inclination  $i$ , the axis ratio  $q$ , the strength  $\theta_E$ , the core radius  $r_c$ , and the slope  $\gamma'$ . In the last row we give the mass-to-light ratio for the baryonic component. Since we have only seven data points with huge uncertainties and vary six parameters in this model, we get also a large range of parameter values within  $1\text{-}\sigma$ . The corresponding  $\chi^2$  is 0.25. Note that we do not obtain any constraints on the anisotropy or inclination, given the assumption of a prior range of  $\beta \in [-0.3, +0.3]$  and  $i \in [0, +0.3]$ .

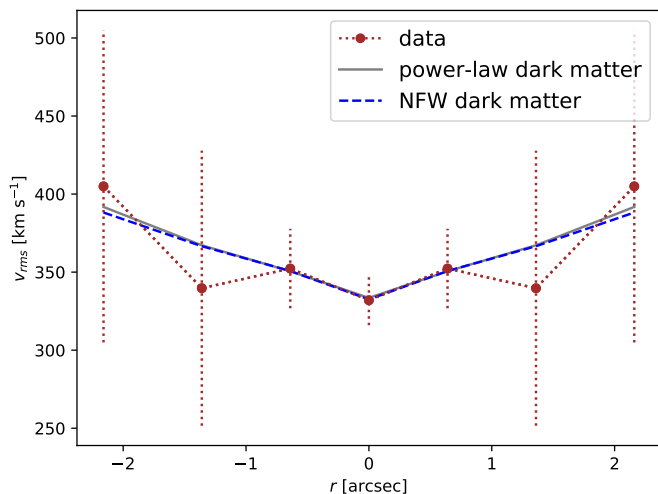


Fig. 7: Values for the second velocity moments  $v_{\text{rms}}$  obtained by adopting the power-law dark matter distribution (solid gray) or NFW (dashed blue) for dynamics-only. In brown are shown the measured data points with the full error bars.

## 6. Dynamical and lensing modeling

After modeling the inner mass distribution of the Cosmic Horseshoe lens galaxy based on lensing-only (Sec. 4) and dynamics-only (Sec. 5), we now combine both approaches. In the last years huge effort has been spent to combine lensing and dynamics for strongly lensed observations to get a more robust mass model (e.g., Treu & Koopmans 2002, 2004; Mortlock & Webster 2000; Gavazzi et al. 2007; Barnabè et al. 2009; Auger et al. 2010; Barnabè et al. 2011; Sonnenfeld et al. 2012; Grillo et al. 2013; Lyskova et al. 2018). Since strong lensing has normally the constraints at the Einstein radius  $r \approx \theta_E$ , which is in our case  $\approx 5''$ , and kinematic measurements are normally in the central region around the effective radius (here  $r \lesssim 2''$ ), one combine information at different radii with these two approaches. This will result in a better constrained model and one might break parameter degeneracies thanks to the complemen-

tary of these two approaches. However, in our particular lens system, we also use the radial arc as lensing constraints in the inner regions.

Although using the *HST* surface brightness observations would provide more lensing constraints, we consider here only the refined image positions presented in Sec. 4.4. The reason for this choice is that we would otherwise overwhelm the 7 data points from dynamics with more than  $10^5$  surface brightness pixel from the images. The data points coming from the identified image positions are still higher, but at the same order of magnitude. Moreover, with this method we are able to weight the contribution of the radial arc and its counter image more.

When we combine dynamics and lensing, we consider again models with and without radial arc, each adopting power-law or NFW dark matter distribution, and all four versions with the full uncertainty of the kinematic data as well as with 5% as a forecast. Additionally, we treat all models with one single  $M/L$  ratio as well as with different  $M/L$  ratios as already done for lensing-only (see Sec. 4.2.1 for details). Based on the same arguments as for the lensing-only, we treat also models by replacing the PSF-like central component (shown in red in Fig. 4) by a point mass.

### 6.1. Three chameleon mass profiles

By combining lensing and dynamics we consider different composite mass model. As first, we use the lens light, which is composed by three chameleon profiles as obtained in Sec. 4.2.1, scaled by a constant mass-to-light ratio as baryonic component. Under this assumption, the best-fit has, when using a power-law dark matter mass distribution, a  $\chi^2$  of 25.08, and, when using a NFW dark matter distribution, a  $\chi^2$  of 71.54. The  $\chi^2$  values reveal that the NFW is not as good at describing the observation as the power-law profile. However, assuming a power-law dark matter distribution, the  $M/L$  value for scaling all three light components is around  $0.1M_\odot/L_\odot$ . This is unphysically low and results in a very high the dark matter fraction.

The next step to model the baryonic component is to allow different mass-to-light ratios for the different light components shown in Fig. 4. This allows us to fit remarkably better with the NFW profile, while we do not get much improvement adopting a power-law dark matter distribution. However, this method does not allow us to obtain meaningful models, as the central component needs an unphysically low  $M/L$ . Therefore, we infer that we cannot assume a mass-to-light ratio for the central component, irrespective of the dark matter distribution.

### 6.2. Point mass and two chameleon mass profiles

As noted in Sec. 4.4.2, the central component is probably associated with an AGN, since its light profile width is similar to the width of the PSF (see Fig. 4) and its  $M/L$  was very low from the previous model in Sec. 6.1. Thus, assuming a mass-to-light ratio for this component would not be physically meaningful and we supersede it by a point mass in the range of a black hole mass. From our previous models and from the fact that the lens galaxy is very massive, we expect this point mass to be comparable to that of a supermassive black hole. For the two other light components we still assume the two fitted chameleon profiles scaled by a  $M/L$ , either the same  $M/L$  for both components, or a different  $M/L$  for each component. Moreover, we test the effect of relaxing the scale parameter  $r_s$  of the NFW profile. It turn out to be

very similar to the model by assuming a fixed value, as expected, such that we present only plots of the model with free  $r_s$ .

We see by comparison of the different models with the point mass that both dark matter profiles result in a similar  $\chi^2$  value (see Table 6). Both dark matter distributions seem to fit the observation with an acceptable dark matter fraction between 60% and 70%. The corresponding plot is shown in Fig. 8 for the final models:

- lensing & dynamics, power-law dark matter, without radial arc
- lensing & dynamics, power-law dark matter, with radial arc
- lensing & dynamics, NFW dark matter, without radial arc
- lensing & dynamics, NFW dark matter, with radial arc

The dark matter fraction is defined here as the dark matter divided by the sum of baryonic matter from the scaled lens light and dark matter enclosed in the radius  $r$ . To be noted is that the point mass is not assumed to be pure baryonic matter, and thus not included in the baryonic component in the calculation. This results in the profile of dark matter fraction having a concave curve in the very central region. Including the point mass with less than  $10^{10} M_\odot$  would shift the fraction insignificantly to lower values. The best-fit parameter values for these four models are given with the corresponding median values with  $1\sigma$  uncertainties in Table 7 (adopting power-law dark matter distribution) and Table 8 (adopting NFW with free scale radius  $r_s$ ).

Table 6: Overview of the different final best-fit models with the point-mass component representing the innermost light component (red profile in Fig. 4).

DM profile	radial arc		one $M/L$		two $M/L$	
	with	without	$\chi^2$	$\chi^2_{\text{red}}$	$\chi^2$	$\chi^2_{\text{red}}$
power-law	✓		21.65	0.84	20.71	0.83
		✓	19.90	0.91	19.58	0.94
NFW	✓		20.14	0.78	19.95	0.80
		✓	19.87	0.91	19.53	0.93

Allowing two independent  $M/L$  seems not to decrease the  $\chi^2$  notably, and we see from the sampling that the outer  $M/L$  is not well constrained and highly degenerate with the other mass components. This might come from the flatness of the profile (see green line in Fig. 4) and less constraints on the outer part where the profile is dominant.

In all models, we can fit very well to the kinematic data with a dynamics- $\chi^2$  of around 0.5. This can be seen in Fig. 9 and is expected because of the large uncertainties and small number of data points available. According to that, we see from Table 7 and Table 8 that we cannot well constrain the anisotropy  $\beta$  and inclination  $i$  given a prior range of  $\beta \in [-0.3, 0.3]$  and  $i \in [0, 0.3]$ . Moreover, from those two tables we see that the radial arc definitely helps to constrain the model better based on the  $1\sigma$  values. Especially parameters which are associated with the central region (e.g., the point mass) are much better constrained using the radial arc.

Additionally we compare the mean convergence  $\bar{\kappa}$  curves of our different models. In Fig. 10 we show the effect of including the radial arc among the constraints in the case of the power-law dark matter distribution (left) or NFW dark matter distribution (right) for the dark matter component and in Fig. 11 for both

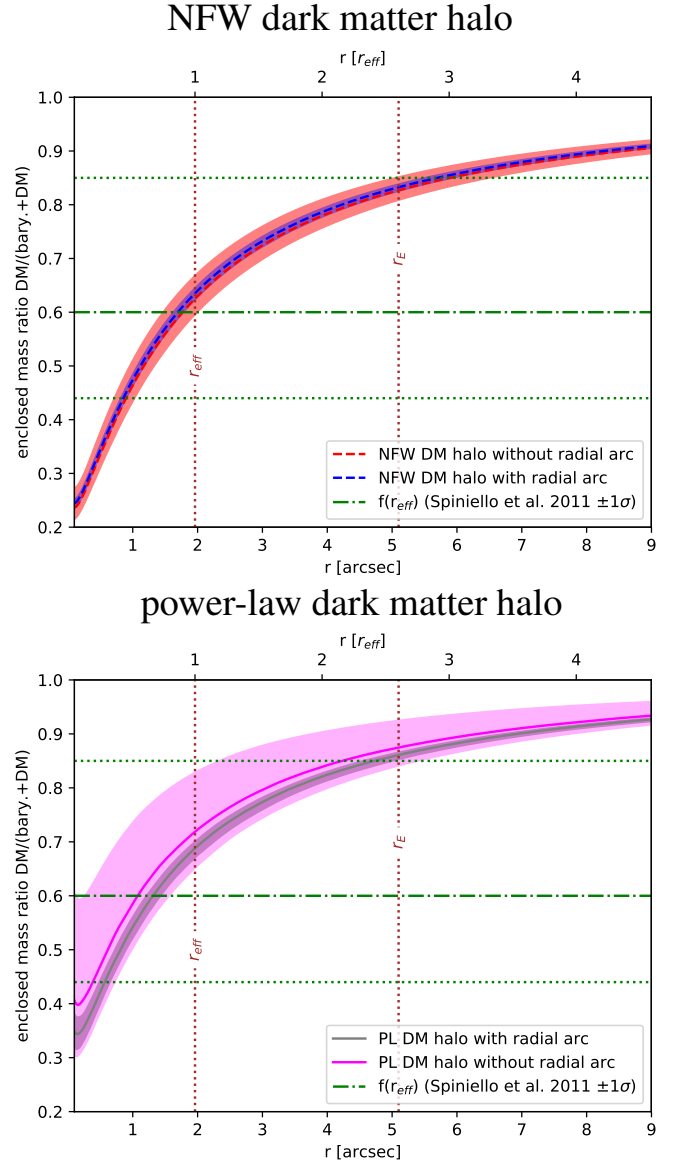


Fig. 8: Enclosed dark matter fraction, i.e. dark matter divided by the sum of baryonic matter from the scaled lens light and dark matter enclosed in radius  $r$ , of the models adopting a power-law (bottom) or NFW (top) dark matter distribution. All models include the point mass in the lens center, which is not considered among the baryonic mass and thus not shown in this plot. For comparison, the value of the dark matter fraction within one effective radius of Spiniello et al. (2011) is shown by the horizontal solid line (for the value) and dashed lines (for  $1\sigma$  uncertainties).

baryonic and dark matter component. We can see that the  $\bar{\kappa}_{\text{tot}}$  are very similar in both cases. In both plots we see the good improvement if we include the radial arc. However, if we compare the NFW and the power-law for the dark matter component, we can see a slight difference in the inner regions. The NFW profile looks less steep.

Indeed, Fig. 12 shows the logarithm of the slope of the dark matter profile  $d \log(\bar{\kappa}_{\text{DM}})/d \log(r)$ . On the left hand panel, we compare the NFW and power-law models including the radial arc while the right hand side shows those excluding the radial arc as constraint. We see that the inferred slope at the Einstein ring is well constrained and independent of the adopted profile.

Table 7: Power-law dark matter halo model: Best-fit and marginalized parameter values for the mass model based on our image positions shown in Fig. 6 and the stellar kinematic data  $v_{\text{rms, sym}}$  given in Table 4.

component	parameter	with radial arc		without rad. arc	
		best-fit	marginalized	best-fit	marginalized
kinematics	$\beta$	0.00	$-0.04^{+0.2}_{-0.2}$	-0.02	$-0.06^{+0.4}_{-0.3}$
	$i$	0.15	$0.11^{+0.07}_{-0.08}$	0.3	$0.2^{+0.2}_{-0.2}$
dark matter (power-law)	$q$	0.91	$0.91^{+0.02}_{-0.02}$	0.90	$0.91^{+0.04}_{-0.05}$
	$\theta_E$ ["]	1.69	$1.66^{+0.07}_{-0.07}$	1.7	$1.7^{+0.3}_{-0.4}$
	$r_c$ ["]	$\equiv 10^{-4}$	–	$\equiv 10^{-4}$	–
	$\gamma'$	1.28	$1.26^{+0.04}_{-0.04}$	1.26	$1.3^{+0.1}_{-0.1}$
shear	$\gamma_{\text{ext}}$	0.077	$0.076^{+0.007}_{-0.006}$	0.08	$0.07^{+0.03}_{-0.02}$
	$\phi_{\text{ext}}$	2.81	$2.80^{+0.04}_{-0.04}$	2.8	$2.8^{+0.1}_{-0.1}$
baryonic matter	$M/L [M_{\odot}/L_{\odot}]$	1.8	$1.9^{+0.2}_{-0.1}$	1.7	$1.7^{+0.6}_{-0.7}$
	$\log(\theta_{E, \text{point}})$	-1.01	$-1.09^{+0.08}_{0.3}$	-2.0	$-2.4^{+1.3}_{-1.6}$

Note. The parameters are the anisotropy  $\beta$ , the inclination  $i$ , the axis ratio  $q$ , the strength  $\theta_E$ , the core radius  $r_c$ , the slope  $\gamma'$ , the shear magnitude  $\gamma_{\text{ext}}$ , and the shear orientation  $\phi_{\text{ext}}$ . Additionally, we give the mass-to-light ratio  $M/L$ , and the strength of the point mass  $\theta_{E, \text{point}}$  in logarithmic scale (i.e.  $-1$  corresponds to around  $10^{10} M_{\odot}$ ).

 Table 8: NFW dark matter halo model: Best-fit and marginalized parameter values for the mass model based on our image positions shown in Fig. 6 and the stellar kinematic data  $v_{\text{rms, sym}}$  given in Table 4.

component	parameter	with radial arc		without rad. arc	
		best-fit	marginalized	best-fit	marginalized
kinematics	$\beta$	0.06	$0.0^{+0.2}_{-0.2}$	-0.1	$-0.08^{+0.2}_{-0.2}$
	$i$	0.10	$0.10^{+0.07}_{-0.07}$	0.2	$0.1^{+0.1}_{-0.1}$
dark matter (NFW)	$q$	0.95	$0.95^{+0.01}_{-0.01}$	0.95	$0.95^{+0.01}_{-0.01}$
	$\theta_E$ ["]	0.63	$0.64^{+0.03}_{-0.02}$	0.62	$0.64^{+0.04}_{-0.03}$
	$r_s$ ["]	185	$170^{+22}_{-28}$	177	$180^{+18}_{-23}$
shear	$\gamma_{\text{ext}}$	0.08	$0.08^{+0.01}_{-0.01}$	0.08	$0.08^{+0.01}_{-0.01}$
	$\phi_{\text{ext}}$	2.81	$2.80^{+0.03}_{-0.04}$	2.82	$2.80^{+0.08}_{-0.05}$
baryonic matter	$M/L [M_{\odot}/L_{\odot}]$	2.2	$2.3^{+0.2}_{-0.1}$	2.5	$2.4^{+0.3}_{-0.4}$
	$\log(\theta_{E, \text{point}})$	-1.01	$-1.10^{+0.08}_{-0.2}$	-1.02	$-2.0^{+0.9}_{-1.3}$

Note. The parameters are the anisotropy  $\beta$ , the inclination  $i$ , the axis ratio  $q$ , the strength  $\theta_E$ , the scale radius  $r_s$ , the shear magnitude  $\gamma_{\text{ext}}$ , and the shear orientation  $\phi_{\text{ext}}$ . Additionally, we give the mass-to-light ratio  $M/L$ , and the strength of the point mass  $\theta_{E, \text{point}}$  in logarithmic scale (i.e.  $-1$  corresponds to around  $10^{10} M_{\odot}$ ).

Including the radial arc, we are able to constrain the slope near the radial arc better to a range of  $\sim -0.3$  to  $\sim -0.15$  at the radial arc radius, covering the spread between the two models. More information in the central region (of  $\sim 1''$ ), such as spatially resolved kinematics, would be required to break further the model degeneracies in measuring the dark matter profile slope in this region.

Finally, to further see the contribution of the radial arc we show the probability density distribution of our final best-fit models. In particular, Fig. 13 shows the power-law models, while Fig. 14 shows the NFW models. From those figures we also see that parameters are much better constrained when radial arc is included, especially the point mass parameter, which is understandable as it is only present in the central region where the radial arc is observed. The prior range of the point mass

strength is for all models the same as we restrict it to be in-between  $10^8 - 10^{10} M_{\odot}$  as known mass range of black holes. This corresponds to  $\log(\theta_{E, \text{point}})$  between  $-4$  and  $-1$ s. We see from this distribution that the radial arc forces the point mass to its upper limit. Since the lens galaxy is very massive, a supermassive black hole is realistic. Interestingly, also the mass-to-light ratio is better constrained by including the radial arc. This confirms the importance of including the radial arc as constraint. We also see that the contribution of the constraints coming from dynamics is quite small, probably due to the small amount of data and the large uncertainties.

We also consider all models under the assumption of 5% uncertainty as the current errors are very huge. Comparing to the figure obtained with the real uncertainties, we do not see a remarkable difference. The uncertainties do not seem to reduce



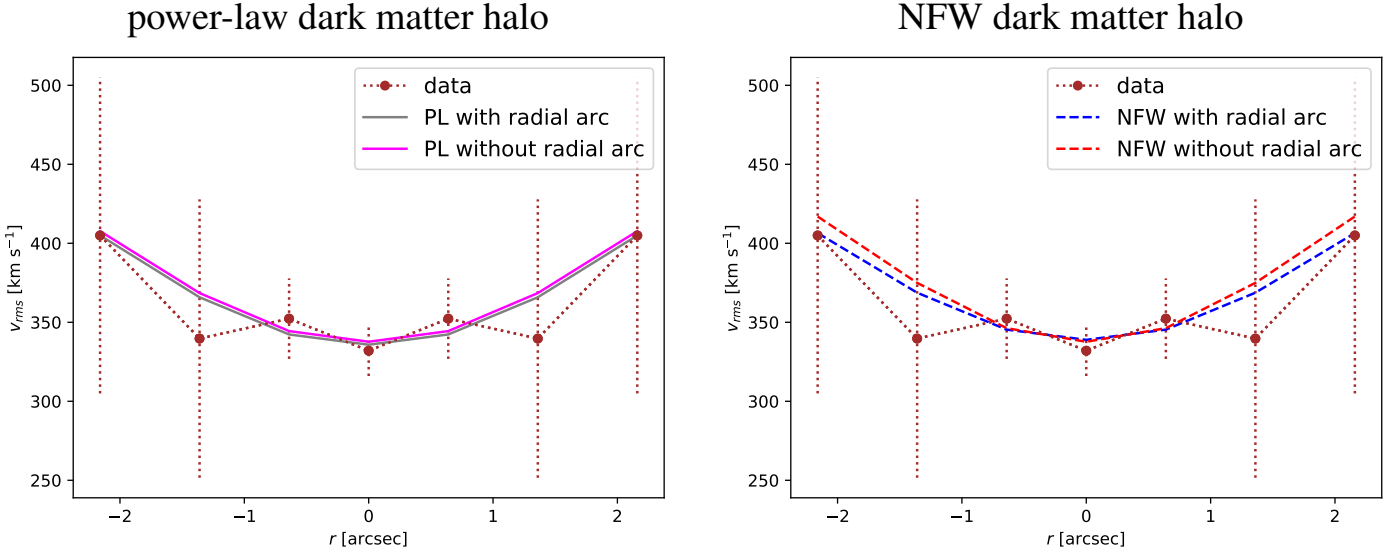


Fig. 9: Values for the second velocity moments  $v_{\text{rms}}$  obtained by adopting the power-law dark matter distribution (left) or NFW (right) for dynamics and lensing. We use here the full uncertainties on the kinematic measurements and the point mass instead of the central component of the fitted light. In brown are shown the measured data points with the error bars.

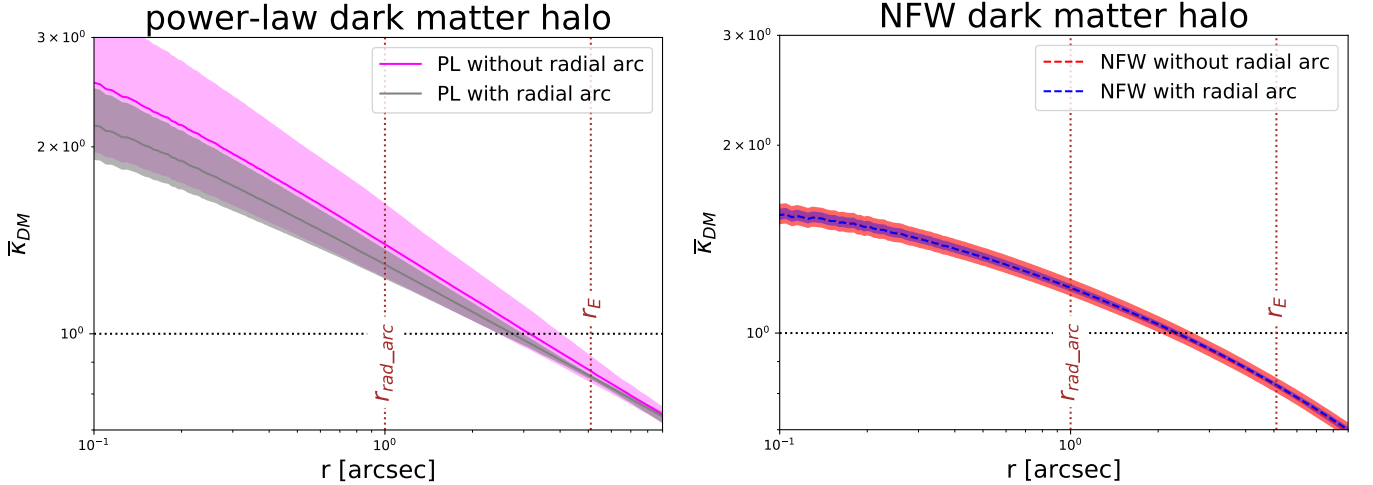


Fig. 10: Mean convergence  $\bar{\kappa}$  of the model with power-law dark matter component (left) or NFW dark matter component (right), with radial arc and without radial arc as constraint. We show the mean corresponding to the  $1\text{-}\sigma$  uncertainty for the dark matter component. We see directly that the radial arc helps to constrain the  $\bar{\kappa}(r)$  curve. The brown line indicates the Einstein radius  $r_E$  and radial arc radius  $r_{\text{rad\_arc}}$ , respectively, and the black line represents the line  $\bar{\kappa} = 1$ .

the parameter space substantially, even though the  $\chi^2$  is higher. Therefore, to further improve the mass modeling through dynamics, spatially resolved kinematic measurements would likely be needed in the future.

## 7. Summary and Conclusion

While in the standard CDM model the structure of dark matter is well understood through large numerical dark matter only simulations (e.g. Dubinski & Carlberg 1991; Navarro et al. 1996a,b), one has to include the baryonic component to reach more complex, but realistic models. Since the deflection of light depends on the total matter, strong gravitational lensing provides a good opportunity to obtain the distribution of the lens' mass. In this paper we study the matter distribution of a unique strong lensing observation, known as the Cosmic Horseshoe (J1148+1930).

This observation shows a radial arc at a redshift of  $z_{s,r} = 1.961$  inside the huge Einstein ring, whose redshift we measured based on spectroscopic observations presented in this paper. Including that radial arc in our models helps to improve our model as it gives lensing constraints in the central region. For obtaining a self-consistent mass model, we include kinematic measurements of the lens galaxy in our final model.

Before disentangling dark matter and baryonic mass, we first construct a model of the total lens mass. Based on this model, we create a composite model with baryonic and dark matter components separately. We adopt different dark matter profiles, a power-law profile, a NFW profile, or a generalization of the NFW profile. For the baryonic component we adopt the lens light distribution, which is described by three components, scaled by a mass-to-light ratio. As one component is very peaky and thus AGN-like, we suggest in our final model to supersede

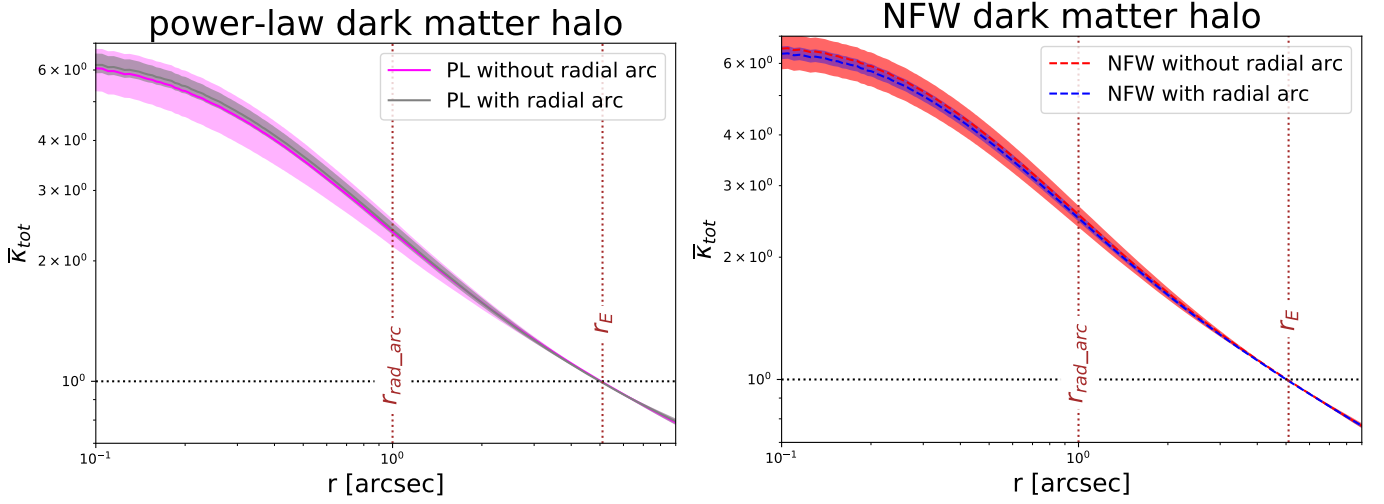


Fig. 11: Mean convergence  $\bar{\kappa}_{\text{tot}}$  of the model with power-law dark matter component (left) or NFW dark matter component (right), with radial arc and without radial arc as constraint. We show the mean corresponding to the  $1-\sigma$  uncertainty for baryonic and dark matter component. We see directly that the radial arc helps to constrain the  $\bar{\kappa}_{\text{tot}}(r)$  curve. The brown line indicates the Einstein radius  $r_E$  and radial arc radius  $r_{\text{rad\_arc}}$ , respectively, and the black line represents the line  $\bar{\kappa}_{\text{tot}} = 1$ .

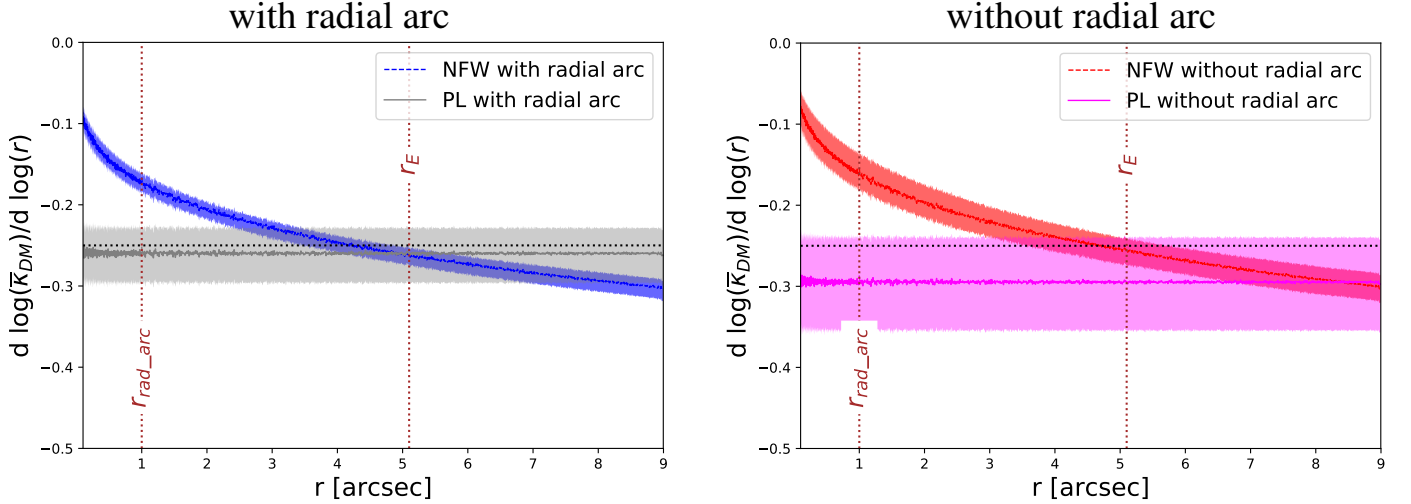


Fig. 12: Radial slope of dark matter profile,  $d \log(\bar{\kappa}_{\text{DM}})/d \log(r)$ , for the models with radial arc (left) and without radial arc (right) as constraint. We show the mean corresponding to the  $1-\sigma$  uncertainty. We see directly that lensing tightly constrains the slope at the Einstein radius, and also the improvement coming from the radial arc. The brown vertical lines indicate the Einstein radius  $r_E$  and radial arc radius  $r_{\text{rad\_arc}}$ , respectively, and the black horizontal line represents the line  $d \log(\bar{\kappa}_{\text{DM}})/d \log(r) = 0.25$  for comparison.

this component by a point mass as we cannot assume a physical meaningful  $M/L$  value. The other two components are still scaled by a mass-to-light ratio. We then include stellar kinematic information of the lens, thanks to which we are able to construct a self-consistent mass model. As we are also interested to see the improvement coming from the radial arc, we always model with and without radial arc and compare those models. From our study of the matter distribution we obtain the following key results:

- Since the width of the central component of the fitted lens light is comparable with the PSF width (compare Fig. 4) and the lens galaxy emits in the radio wavelengths, our modeling results support a mass model for the Cosmic Horseshoe lens galaxy with a point component in the center instead of a luminous component scaled by a mass-to-light ratio. The

two outer components are scaled with a mass-to-light ratio to account for the baryonic mass. The dark matter component could follow either a power-law or an NFW profile, since both profiles could adequately fit to the current data.

- We can construct a better mass model thanks to the contribution of radial arc and its counter image. Thus we infer the radial arc is part of the full Cosmic Horseshoe system. It turns out that the radial arc improves the dark matter halo parameter constraints independently of the adopted dark matter distribution.
- When adding the contribution of dynamical modeling, we find that actually this method is not able to constrain significantly better the possible parameter range. We suspect this might be due to the lack of data points and large uncertainties. When using the forecasted 5% uncertainties on the

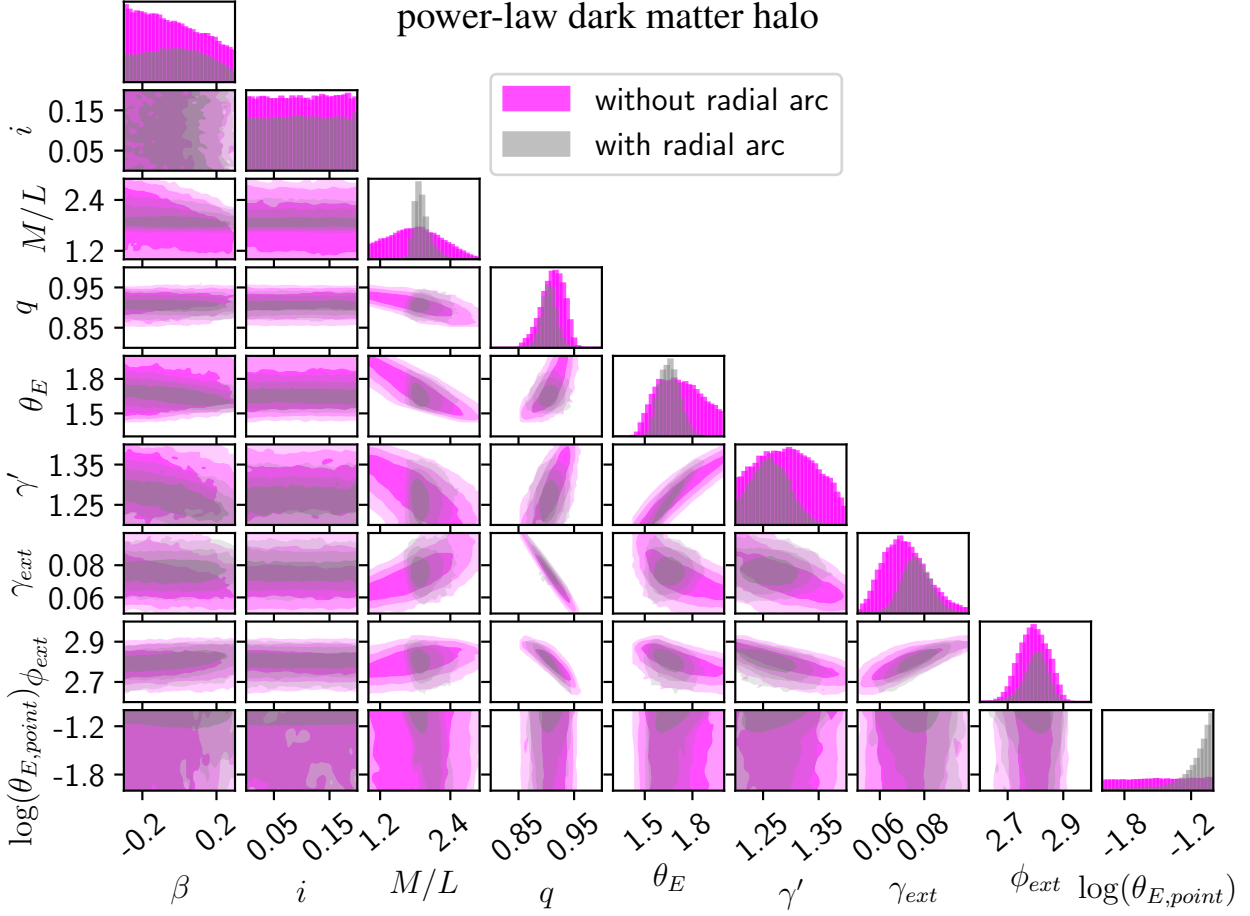


Fig. 13: Probability density distribution for our best-fit models, adopting a power-law dark matter profile. In the diagonal one sees the 1-D histograms for the corresponding parameter given on the  $x$ -axis (and independent of the label in the  $y$ -axis), while below in the triangle the joint 2-D probability distributions corresponding to the parameters given on  $x$ - and  $y$ -axis are shown. The different opacities in the 2-D plots indicate the different sigma ranges. In general, one sees that the model with radial arc is much better constrained than without. The parameters are the anisotropy  $\beta$ , the inclination  $i$ , the shear magnitude, and its orientation counter clockwise to the  $x$ -axis, for the dark matter profile the axis ratio  $q$ , Einstein angle  $\theta_E$ , and the slope  $\gamma'$ . Additionally, we show the mass-to-light ratio  $M/L$ , which is used to scale the two light components, and the logarithm of the strength of the point mass  $\theta_{E,\text{point}}$ . The prior range for the point mass is set to  $10^8 - 10^{10} M_\odot$  as the known limits of black holes, corresponding to  $\log(\theta_{E,\text{point}})$  between  $-4$  and  $-1$ .

kinematic measurements, we constrain the parameter ranges slightly better.

- When trying to model the baryonic matter independently of the dark matter, we consider two scenarios: the matter aligned with the lens light or to be  $90^\circ$  offset. Here we find that the model with the  $90^\circ$  rotated orientation fits better. Thus, the major axis of the projected halo mass distribution seem to be perpendicular to the major axis of the baryonic mass distribution.
- For all the tested models, we obtain a mass of around  $5.2 \times 10^{12} M_\odot$  enclosed in the Einstein ring. This is in agreement with previous studies of the Cosmic Horseshoe, e.g., Dye et al. (2008). We predict the dark matter fraction at one effective radius to be 0.65, whose value is slightly higher as predicted by Spiniello et al. (2011), but within their  $1\sigma$  range. The exact fraction depends also on the specific model.

From this work, we demonstrate the utility of having a radial arc in constraining the dark matter profile, particularly in the inner regions. This is important for the future, when we might discover more lenses in current and future surveys. New single-galaxy lens systems with radial arcs would provide great opportunities to model the inner dark matter distributions and probe galaxy formation scenarios. This would also give a more general statement rather than from one anecdotal example.

Moreover, we see that combining lensing and kinematic data helps to constrain the model better, even though current kinematic data of the Cosmic Horseshoe are limited. Thus further kinematic measurements, particularly if spatially resolved, of such strong lens observations would help to construct a better mass model.

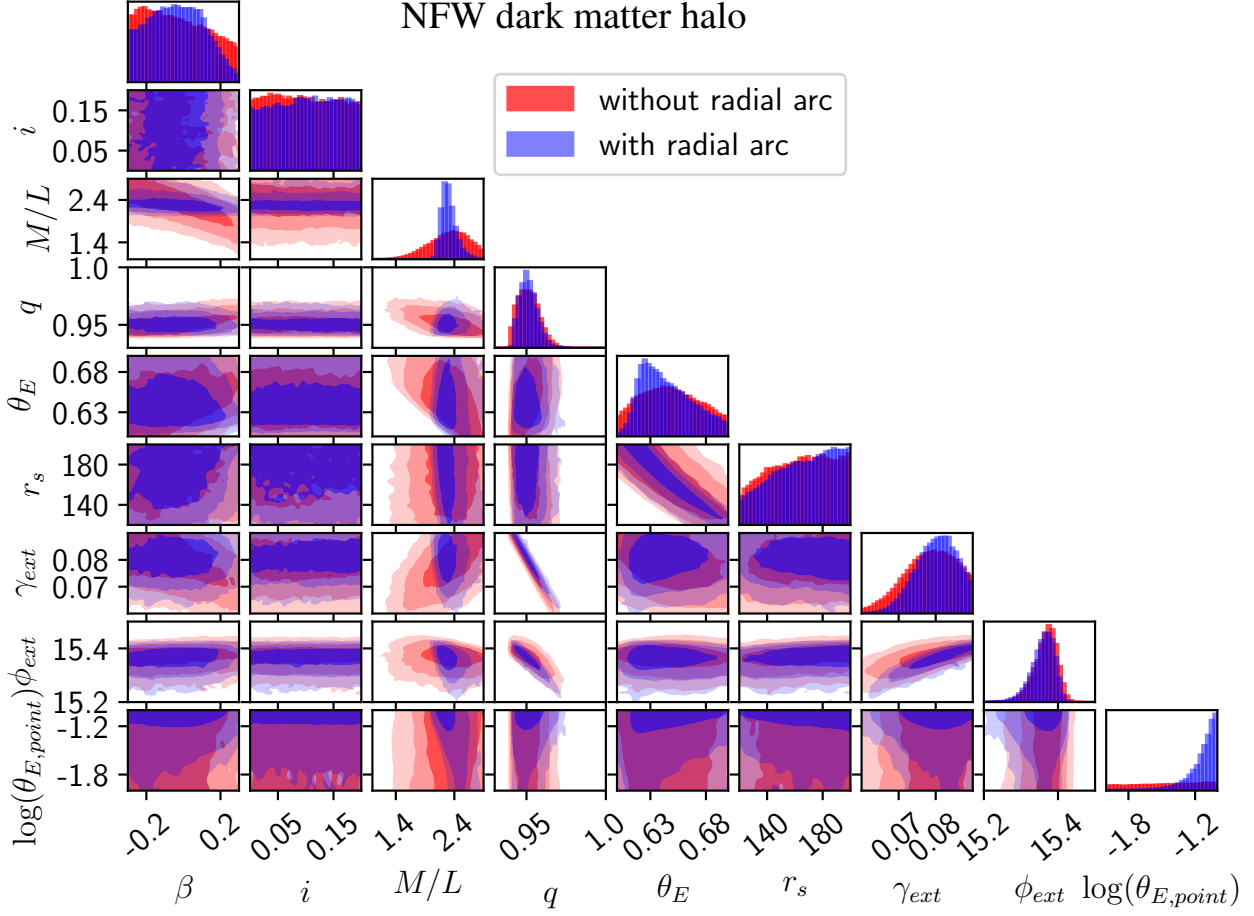


Fig. 14: Probability density distribution for our best-fit models, adopting a NFW dark matter profile. In the diagonal one sees the 1-D histograms for the corresponding parameter given on the  $x$ -axis (and independent of the label in the  $y$ -axis), while below in the triangle the joint 2-D probability distributions corresponding to the parameters given on  $x$ - and  $y$ -axis are shown. The different opacities in the 2-D plots indicate the different sigma ranges. In general, one sees that the model with radial arc is much better constrained than without. The parameters are the anisotropy  $\beta$ , the inclination  $i$ , the shear magnitude, and its orientation counter clockwise to the  $x$ -axis, for the dark matter profile the axis ratio  $q$ , strength (right)  $\theta_E$ , and the scale radius  $r_s$ . Additionally, we show the mass-to-light ratio  $M/L$ , which is used to scale the two light components, and the logarithm of the strength of the point mass  $\theta_{E,\text{point}}$ . The prior range for the point mass is set to  $10^8 - 10^{10} M_\odot$  as the known limits of black holes, corresponding to  $\log(\theta_{E,\text{point}})$  between  $-4$  and  $-1$ .

*Acknowledgements.* We thank M. Auger for useful discussions.

SS, GC, SHS and AY thank the Max Planck Society for support through the Max Planck Research Group for SHS. This research was supported in part by Perimeter Institute for Theoretical Physics. Research at Perimeter Institute is supported by the Government of Canada through the Department of Innovation, Science and Economic Development and by the Province of Ontario through the Ministry of Research, Innovation and Science.

The analysis is based on: 1) observations made with the NASA/ESA *Hubble Space Telescope*, obtained at the Space Telescope Science Institute, which is operated by the Association of Universities for Research in Astronomy, Inc., under NASA contract NAS 5-26555. These observations were done in May 2010 with Proposal ID 11602 and in November 2011 with Proposal ID 12266; 2) Observations obtained at the Gemini Observatory, which is operated by the Association of Universities for Research in Astronomy, Inc., under a cooperative agreement with the NSF on behalf of the Gemini partnership: the National Science Foundation (United States), the National Research Council (Canada), CONICYT (Chile), Ministerio de Ciencia, Tecnología e Innovación Productiva (Argentina), and Ministério da Ciência, Tecnologia e Inovação (Brazil).

## References

- Abadi, M. G., Navarro, J. F., Fardal, M., Babul, A., & Steinmetz, M. 2010, *MNRAS*, 407, 435  
 Abazajian, K., Fuller, G. M., & Patel, M. 2001, *Phys. Rev. D*, 64, 023501  
 Auger, M. W., Treu, T., Bolton, A. S., et al. 2010, *ApJ*, 724, 511  
 Barkana, R. 1998, *ApJ*, 502, 531  
 Barnabè, M., Czoske, O., Koopmans, L. V. E., Treu, T., & Bolton, A. S. 2011, *MNRAS*, 415, 2215  
 Barnabè, M., Czoske, O., Koopmans, L. V. E., et al. 2009, *MNRAS*, 399, 21  
 Bellagamba, F., Tessore, N., & Metcalf, R. B. 2017, *MNRAS*, 464, 4823  
 Belokurov, V., Evans, N. W., Moiseev, A., et al. 2007, *ApJ*, 671, L9  
 Bendenelli, O. 1991, *ApJ*, 366, 599  
 Bernardi, M., Sheth, R. K., Dominguez-Sanchez, H., et al. 2018, *MNRAS*  
 Binney, J. & Mamon, G. A. 1982, *MNRAS*, 200, 361  
 Binney, J. J., Davies, R. L., & Illingworth, G. D. 1990, *ApJ*, 361, 78  
 Blandford, R. & Narayan, R. 1986, *ApJ*, 310, 568  
 Blumenthal, G. R., Faber, S. M., Flores, R., & Primack, J. R. 1986, *ApJ*, 301, 27  
 Bonvin, V., Courbin, F., Suyu, S. H., et al. 2017, *MNRAS*, 465, 4914  
 Cappellari, M. 2002, *MNRAS*, 333, 400  
 Cappellari, M. 2008, *MNRAS*, 390, 71  
 Cappellari, M. & Copin, Y. 2003, *MNRAS*, 342, 345

- Chuzhoy, L. 2006, ArXiv Astrophysics e-prints
- Collett, T. E., Buckley-Geer, E., Lin, H., et al. 2017, ArXiv e-prints
- De Vaucouleurs, G. 1948, 227, 586
- Dekel, A., Ishai, G., Dutton, A. A., & Maccio, A. V. 2017, 468, 1005
- Diemand, J., Zemp, M., Moore, B., Stadel, J., & Carollo, C. M. 2005, MNRAS, 364, 665
- Dubinski, J. & Carlberg, R. G. 1991, ApJ, 378, 496
- Dutton, A. A., Brewer, B. J., Marshall, P. J., et al. 2011, MNRAS, 417, 1621
- Dye, S., Evans, N. W., Belokurov, V., Warren, S. J., & Hewett, P. 2008, MNRAS, 388, 384
- Dye, S. & Warren, S. J. 2005, ApJ, 623, 31
- El-Zant, A., Shlosman, I., & Hoffman, Y. 2001, ApJ, 560, 636
- El-Zant, A. A., Hoffman, Y., Primack, J., Combes, F., & Shlosman, I. 2004, ApJ, 607, L75
- Elias, J. H., Joyce, R. R., Liang, M., et al. 2006, in Proc. SPIE, Vol. 6269, Society of Photo-Optical Instrumentation Engineers (SPIE) Conference Series, 62694C
- Foreman-Mackey, D., Hogg, D. W., Lang, D., & Goodman, J. 2013, PASP, 125, 306
- Gao, L., Navarro, J. F., Frenk, C. S., et al. 2012, MNRAS, 425, 2169
- Gavazzi, R., Treu, T., Koopmans, L. V. E., et al. 2008, ApJ, 677, 1046
- Gavazzi, R., Treu, T., Rhodes, J. D., et al. 2007, ApJ, 667, 176
- Ghigna, S., Moore, B., Governato, F., et al. 2000, ApJ, 544, 616
- Gnedin, O. Y., Kravtsov, A. V., Klypin, A. A., & Nagai, D. 2004, ApJ, 616, 16
- Golse, G. & Kneib, J.-P. 2002, A&A, 390, 821
- Governato, F., Brook, C., Mayer, L., et al. 2010, Nature, 463, 203
- Graham, A. W., Merritt, D., Moore, B., Diemand, J., & Terzić, B. 2006a, AJ, 132, 2701
- Graham, A. W., Merritt, D., Moore, B., Diemand, J., & Terzić, B. 2006b, AJ, 132, 2711
- Grillo, C., Christensen, L., Gallazzi, A., & Rasmussen, J. 2013, MNRAS, 433, 2604
- Gustafsson, M., Fairbairn, M., & Sommer-Larsen, J. 2006, Phys. Rev. D, 74, 123522
- Hasinoff, S. W. 2012
- Jeans, J. H. 1922, MNRAS, 82, 122
- Kaplinghat, M. 2005, Phys. Rev. D, 72, 063510
- Kochanek, C. S. & Rybicki, G. B. 1996, MNRAS, 280, 1257
- Lapi, A. & Cavaliere, A. 2011, ApJ, 743, 127
- Laporte, C. F. P. & White, S. D. M. 2015, MNRAS, 451, 1177
- Li, Y., Ruzsowski, M., & Bryan, G. L. 2017, ApJ, 847, 106
- Lyskova, N., Churazov, E., & Naab, T. 2018, MNRAS, 475, 2403
- Maller, A. H., Simard, L., Guhathakurta, P., et al. 2000, ApJ, 533, 194
- Martizzi, D., Teyssier, R., & Moore, B. 2013, MNRAS, 432, 1947
- Monnet, G., Bacon, R., & Emsellem, E. 1992, A&A, 253, 366
- Mortlock, D. J. & Webster, R. L. 2000, ArXiv Astrophysics e-prints
- Moutarde, F., Alimi, J.-M., Bouchet, F. R., & Pellat, R. 1995, ApJ, 441, 10
- Nagai, R. & Miyamoto, M. 1976, PASJ, 28, 1
- Navarro, J. F., Eke, V. R., & Frenk, C. S. 1996a, MNRAS, 283, L72
- Navarro, J. F., Frenk, C. S., & White, S. D. M. 1996b, ApJ, 462, 563
- Navarro, J. F., Frenk, C. S., & White, S. D. M. 1997, ApJ, 490, 493
- Navarro, J. F., Ludlow, A., Springel, V., et al. 2010, MNRAS, 402, 21
- Nguyen, D. D. 2017, ArXiv e-prints
- Nipoti, C., Treu, T., Ciotti, L., & Stiavelli, M. 2004, MNRAS, 355, 1119
- Pedrosa, S., Tissera, P. B., & Scannapieco, C. 2009, MNRAS, 395, L57
- Peirani, S., Dubois, Y., Volonteri, M., et al. 2017, MNRAS, 472, 2153
- Peirani, S., Kay, S., & Silk, J. 2008, A&A, 479, 123
- Peter, A. H. G., Moody, C. E., & Kamionkowski, M. 2010, Phys. Rev. D, 81, 103501
- Planck Collaboration, Ade, P. A. R., Aghanim, N., et al. 2016, A&A, 594, A13
- Pontzen, A. & Governato, F. 2012, MNRAS, 421, 3464
- Quider, A. M., Pettini, M., Shapley, A. E., & Steidel, C. C. 2009, MNRAS, 398, 1263
- Rantala, A., Johansson, P. H., Naab, T., Thomas, J., & Frigo, M. 2018, ApJ, 864, 113
- Romano-Díaz, E., Shlosman, I., Hoffman, Y., & Heller, C. 2008, ApJ, 685, L105
- Rybicki, G. B. 1987, in IAU Symposium, Vol. 127, Structure and Dynamics of Elliptical Galaxies, ed. P. T. de Zeeuw, 397
- Ryden, B. S. 1991, ApJ, 370, 15
- Samurović, S. 2016, Bulgarian Astronomical Journal, 24, 12
- Satoh, C. 1980, PASJ, 32, 41
- Schneider, P., Kochanek, C., & Wambsganss, J. 2006, Gravitational Lensing: Strong, Weak and Micro - Saas-Fee Advanced Course 33 (Berlin Heidelberg: Springer Science & Business Media)
- Sellwood, J. A. & McGaugh, S. S. 2005, ApJ, 634, 70
- Sérsic, J. L. 1963, Boletín de la Asociación Argentina de Astronomía La Plata Argentina, 6, 41
- Sommer-Larsen, J. & Limousin, M. 2010, MNRAS, 408, 1998
- Sonnenfeld, A., Leauthaud, A., Auger, M. W., et al. 2018, ArXiv e-prints
- Sonnenfeld, A., Treu, T., Gavazzi, R., et al. 2012, ApJ, 752, 163
- Spiegel, D. N. & Steinhardt, P. J. 2000, Physical Review Letters, 84, 3760
- Spiniello, C., Koopmans, L. V. E., Trager, S. C., Czoske, O., & Treu, T. 2011, MNRAS, 417, 3000
- Suyu, S. H. & Halkola, A. 2010, A&A, 524, A94
- Suyu, S. H., Hensel, S. W., McKean, J. P., et al. 2012, ApJ, 750, 10
- Suyu, S. H., Marshall, P. J., Hobson, M. P., & Blandford, R. D. 2006, MNRAS, 371, 983
- Suyu, S. H., Treu, T., Hilbert, S., et al. 2014, ApJ, 788, L35
- Thomas, J., Ma, C.-P., McConnell, N. J., et al. 2016, Nature, 532, 340
- Tonini, C., Lapi, A., & Salucci, P. 2006, ApJ, 649, 591
- Treu, T. 2010, ARA&A, 48, 87
- Treu, T. & Ellis, R. S. 2015, Contemporary Physics, 56, 17
- Treu, T. & Koopmans, L. V. E. 2002, ApJ, 575, 87
- Treu, T. & Koopmans, L. V. E. 2004, ApJ, 611, 739
- van de Ven, G., Falcón-Barroso, J., McDermaid, R. M., et al. 2010, ApJ, 719, 1481
- van der Marel, R. P., Binney, J., & Davies, R. L. 1990, MNRAS, 245, 582
- Wang, W., Han, J., Cole, S., et al. 2018, MNRAS, 476, 5669
- Yıldırım, A., Suyu, S., & Halkola, A. in prep.
- Yıldırım, A., van den Bosch, R. C. E., van de Ven, G., et al. 2016, MNRAS, 456, 538
- Yıldırım, A., van den Bosch, R. C. E., van de Ven, G., et al. 2017, MNRAS, 468, 4216

## 8. Dynamical modeling using Multi-Gaussian-Expansion (MGE) parameterization and Jeans ansatz

Here we introduce briefly the Jeans formalism which we use for dynamical modeling in our mass model of the Cosmic Horseshoe. Since we assume an axisymmetric model, we only consider this specific case here, and refer for details and the general case to Cappellari (2008).

We start from the general axisymmetric Jeans equations (Jeans 1922)

$$\frac{\overline{\mu v_R^2} - \overline{\mu v_\phi^2}}{R} + \frac{\partial(\overline{\mu v_R^2})}{\partial R} + \frac{\partial(\overline{\mu v_R v_z})}{\partial z} = -\mu \frac{\partial \Phi}{\partial R} \quad (18)$$

$$\frac{\overline{\mu v_R v_z}}{R} + \frac{\partial(\overline{\mu v_z^2})}{\partial z} + \frac{\partial(\overline{\mu v_R v_z})}{\partial R} = -\mu \frac{\partial \Phi}{\partial z}, \quad (19)$$

which are only two equations since the third reduces to zero in the axisymmetric case. Here,  $\Phi$  is the gravitational potential,  $(R, z, \phi)$  standard cylindrical coordinates,  $\overline{\mu v_k v_j}$  an abbreviation for  $\int v_k v_j f d^3 v$  with  $f(x, v)$  the distribution function (DF) at position  $x$  and with velocity  $v$  and  $\mu$  the luminosity density (not  $v$  as in Cappellari (2008) to distinguish better from the velocity  $v$ ). One can reduce these two equations to

$$\frac{b \overline{\mu v_z^2} - \overline{\mu v_\phi^2}}{R} + \frac{\partial(b \overline{\mu v_z^2})}{\partial R} = -\mu \frac{\partial \Phi}{\partial R} \quad (20)$$

$$\frac{\partial(\overline{\mu v_z^2})}{\partial z} = -\mu \frac{\partial \Phi}{\partial z} \quad (21)$$

by assuming that the velocity ellipsoid is aligned with the cylindrical coordinate system  $(R, z, \phi)$  and that the anisotropy  $b$  is constant and given by

$$\overline{v_R^2} = b \times \overline{v_z^2}. \quad (22)$$

The situation  $b = 1$  is the so-called semi-isotropic or two-integral case.

For the stellar density and the total density we adopt the *Multi-Gaussian Expansion* (MGE) parameterization (Bendinelli



1991; Monnet et al. 1992) as described in Cappellari (2002) because of its accuracy in reproducing the surface brightness and its robustness. By assuming that the  $x$ -axis is aligned with the photometric major axis, the surface brightness  $\Sigma$  is given by

$$\Sigma(x', y') = \sum_{k=1}^N \frac{L_k}{2\pi\sigma_k^2 q'_k} \exp\left[-\frac{1}{2\sigma_k^2} \left(x'^2 + \frac{y'^2}{q_k'^2}\right)\right] \quad (23)$$

at the position  $(x', y')$  of the plane of sky. Here,  $N$  is the number of adopted Gaussians with luminosity  $L_k$ , observed axis ratio  $q'_k$  between 0 and 1, and dispersion  $\sigma_k$  along the major axis.

Since the galaxies have an unknown inclination  $i$ , one needs a deprojection of the surface brightness to get the intrinsic luminosity density. This is not unique unless one considers edge-on ( $i = 90^\circ$ ) oriented galaxies (Rybicki 1987; Kochanek & Rybicki 1996). As described in Cappellari (2008), one advantage of the MGE method is that one can relatively well include the roundness of the model to get realistic densities and fulfill the *morphological criterion*, which is described in detail in Cappellari & Copin (2003). Thereafter one can write the deprojected MGE oblate axisymmetric luminous density  $\mu$  as

$$\mu(R, z) = \sum_{k=1}^N \frac{L_k}{(2\pi)^{3/2} \sigma_k^3 q_k} \exp\left[-\frac{1}{2\sigma_k^2} \left(R^2 + \frac{z^2}{q_k^2}\right)\right], \quad (24)$$

with the intrinsic axial ratio of each Gaussian component

$$q_k = \frac{\sqrt{q_k'^2 - \cos^2(i)}}{\sin(i)}. \quad (25)$$

As we said, we adopt for the total density  $\rho$  an MGE parameterization as well, such that one can write it as a sum of  $M$  Gaussians:

$$\rho(R, z) = \sum_{j=1}^M \frac{M_j}{(2\pi)^{3/2} \sigma_j^3 q_j} \exp\left[-\frac{1}{2\sigma_j^2} \left(R^2 + \frac{z^2}{q_j^2}\right)\right]. \quad (26)$$

After applying the MGE formalism to the solution of axisymmetric anisotropic Jeans equations 20 and 21, i.e. one substitutes Eq. 24 and the gravitational potential obtained from Eq. 26 into equations 20 and 21, then one can perform the integral analytically. With that, one can integrate along the line-of-sight (LOS) to obtain the observables which we then want to compare to the galaxy kinematics. These are the total observed second moment and the first moment. For the last one, we need additional assumptions because one has to decide how the second moment separates into the contribution of ordered and random motion, which is defined by

$$\overline{v_\phi^2} = \overline{v_\phi}^2 + \sigma_\phi^2, \quad (27)$$

or in simplified, but often used notation

$$v_{\text{rms}}^2 = v^2 + \sigma^2. \quad (28)$$

Here  $v_{\text{rms}}$  is the second velocity moment,  $v$  the rotation, and  $\sigma$  the velocity dispersion. These necessary additional assumptions are the reason why one considers often the second velocity moment, which is the more general formula. However, the first moment are very useful to quantify the amount of rotation in galaxies and are thus sometimes used (e.g., Nagai & Miyamoto 1976; Satoh 1980; Binney et al. 1990; van der Marel et al. 1990).

In the case that the anisotropy  $b_k$  is different for each Gaussian, the total luminosity-weighted anisotropy of an MGE

model, under the assumptions noted above, is given by the definition (Binney & Mamon 1982; Cappellari 2008)

$$\beta_z(R, z) \equiv 1 - \frac{\overline{v_z^2}}{v_R^2} = 1 - \frac{\sum_{k=1}^N [\mu \overline{v_z^2}]_k}{\sum_{k=1}^N b_k [\mu v_z^2]_k}. \quad (29)$$

For further theoretical discussion we refer the reader to the paper Cappellari (2008).